Small-Scale Topography of 433 Eros from Laser Altimetry and Imaging

Andrew F. Cheng, O. Barnouin-Jha, and L. Prockter

The Johns Hopkins University Applied Physics Laboratory, Laurel, Maryland 20723
E-mail: andrew.cheng@jhuapl.edu

M. T. Zuber and G. Neumann

Massachusetts Institute of Technology, Cambridge, Massachusetts 02139

D. E. Smith and J. Garvin

NASA/Goddard Space Flight Center, Greenbelt, Maryland 20771

M. Robinson

Northwestern University, Evanston, Illinois 60208

and

J. Veverka and P. Thomas

Cornell University, Ithaca, New York 14853

The NEAR laser rangefinder (NLR) obtained more than 16 million range returns from asteroid 433 Eros. We present the first results from analyses of topographic profiles interpreted with the aid of simultaneous, boresighted images obtained by the NEAR multispectral imager (MSI). The location of the NLR boresight relative to that of MSI is determined by detailed correlations of ranging data and simultaneous images, including cases where the laser boresight slewed off and on the limb of the asteroid and cases where the laser illuminated a boulder close to the time of an image. In the data presented, the precision of the range measurements is about 1 m, with the minimum spot diameter under 5 m, and successive spots are contiguous or overlapping. Elevation on the irregular object Eros is given with respect to the gravitational and centrifugal potential. Landslides in craters are characterized. Possible crater benches are identified. Examples of infilled craters are presented. These observations suggest a depth of unconsolidated regolith, which is subject to sliding, of typically a few tens of meters. An example of structurally controlled cratering is presented. Examples of tectonic features are described. Surface roughness on Eros is approximately self-affine from scales of a few meters to hundreds of meters. A comparison of fractal statistics shows that Eros is extremely rough on observed scales, when compared to terrestrial a'a lava on submeter scales and undisturbed lunar regolith on subcentimeter scales.   © 2002 Elsevier Science (USA)

Key Words: asteroid surfaces; asteroids; Eros; regoliths; tectonics.

1. INTRODUCTION

The Near Earth Asteroid Rendezvous (NEAR) spacecraft, the mission of which is to perform the first comprehensive orbital study of an asteroid (Cheng *et al.* 1997), was launched on February 17, 1996 and performed the first flyby of a C-type main belt asteroid, 253 Mathilde, on June 27, 1997 (Veverka *et al.* 1997a, Yeomans *et al.* 1997). After a flyby of Eros in December, 1998 (Yeomans *et al.* 1999, Veverka *et al.* 1999), NEAR entered orbit on February 14, 2000 around its primary mission target, the near-Earth asteroid 433 Eros. The spacecraft has subsequently been renamed NEAR Shoemaker in honor of Eugene M. Shoemaker (1928–1997).

NEAR is a three-axis stabilized spacecraft that carries a five-instrument scientific payload. This paper reports results of coordinated observations by two instruments, the NEAR laser rangefinder (NLR) and the multispectral imager (MSI). The scientific background and expected results of these investigations on NEAR were summarized in a special issue of the *Journal of Geophysical Research* (Zuber *et al.* 1997, Veverka *et al.* 1997b). NLR measures the range between the spacecraft and a spot on the surface of Eros by measuring the round trip time of flight for a laser pulse. NLR and MSI share a common boresight, so that NLR measures the range to a spot within the field of view (FOV) of MSI. The two instruments have acquired a substantial volume

of simultaneous observations of Eros. Imaging results from the first half of the Eros rendezvous period (February through July, 2000) were reported by Veverka *et al.* (2000), and ranging results from this period were reported by Zuber *et al.* (2000).

At Eros, NLR measures ranges to the surface with a single-shot precision of about 1 m at 40-km range (Cheng *et al.* 2000), which supports the requirement of <6 m accuracy at 50 km (Zuber *et al.* 1997, Cole *et al.* 1997). Precision in this context refers to the repeatability of measurements given random errors, whereas accuracy also includes possible systematic errors from ranging to a rough surface at nonnormal incidence. NLR is a direct-detection, time-of-flight laser altimeter that employs a solid-state, diode-pumped Cr : Nd : YAG laser transmitter at 1064 nm wavelength, a Cassegrain receiver telescope, and a receiver with a silicon avalanche photodiode detector. NLR determines the range from the NEAR spacecraft to the surface of Eros to within a range resolution of 0.312 m (single count), using a 480-MHz time-of-flight counter. Salient instrument characteristics are listed in Table I. NLR is a leading-edge detector, meaning that the time of flight is measured to the time at which the returned signal amplitude rises above the receiver threshold. The measured times of flight, and therefore also the measured ranges, depend weakly on the value of the receiver threshold, and this effect is accounted for in the data analysis. To date, the receiver threshold has been set usually to 64 mV nominal while at ranges >50 km but at 128 mV nominal while at closer ranges, requiring a 40-cm range correction (Cheng *et al.* 2000). Complete descriptions of NLR operational modes, data formats, and in-flight calibration results are given by Cheng *et al.* (2000). Detailed descriptions of instrument characteristics, hardware design, and ground calibration results are given by Cole *et al.* (1997).

NLR does not measure the shape of Eros directly but finds the range from the spacecraft to a spot on the surface of Eros at a given time. To determine shape and topography, this spot must be located accurately relative to Eros body-fixed coordinates to find the Eros latitude and longitude sampled by NLR at the time in question. As is discussed further in Section 3, solutions for the spacecraft location, instrument pointing, and asteroid rotation are all required. To date, the best available spacecraft ephemeredes are uncertain by more than the ∼1-m precision of the range measurements from 50-km orbits. Due to these uncertainties, it is not currently possible to assemble altimetric tracks from times separated by more than a few hours into an Eros digital terrain model (DTM), without making extensive ephemeris corrections to remove inconsistencies at crossovers where the same feature was measured on different occasions (e.g., Neumann *et al.* 2000).

This paper presents results from analyses of short altimetric arcs of <1-h duration. Only relative topography, or height differences characterizing small-scale features on the surface, will be inferred from these data. This is possible because the ephemeris errors vary slowly. Over time spans of <1 h, the ephemeris errors produce overall biases in the topographic profiles, which can be ignored for studies of small-scale topography. The results in this work do not depend on determining the absolute positions of specific features. Over longer time spans, the ephemeris errors can be dealt with statistically to derive global shape models (Zuber *et al.* 2000), but with this approach the small-scale features are not resolved. High-resolution and high-accuracy DTMs of Eros will be the subject of future studies as improved spacecraft ephemerides become available. Stereo images were acquired of some areas on Eros but have not been reduced for the features described in this paper.

The subject of the present work is the small-scale topography of Eros, which bears on fundamental questions about the geology, structure, and evolution of the asteroid (Zuber *et al.* 2000). Accurate measurements of structural features on Eros such as linear grooves and ridges can provide clues to the interior structure of the asteroid and help answer fundamental questions. For example, is Eros a "collisional shard" or is it a "rubble pile?" In the former view, the evolution of Eros is dominated by collisions; the overall shape may have been determined initially by collisional breakup of a parent body but was modified by subsequent collisions large and small (e.g., see the review by Bell *et al.* 1989). For Gaspra, the faceted shape and the presence of grooves may hint at such a collisional picture (Thomas *et al.* 1994). In this case, Eros would be a globally consolidated body with appreciable strength, and self-gravitation would be relatively unimportant. However, an alternative picture is that Eros was thoroughly broken up without being dispersed (or, possibly, Eros reaccreted), so it would now be a rubble pile consisting of much smaller component bodies bound primarily by gravitation (Davis *et al.* 1994, Melosh and Ryan 1997). The iron asteroid 216 Kleopatra, with its "dog bone" shape (Ostro *et al.* 2000) may be a gravitationally bound contact binary. Some small asteroids rotate too rapidly to be gravitationally bound agglomerates (e.g., Ostro *et al.* 1999), but Eros is not among them (Yeomans *et al.* 2000).

TABLE I
NLR Characteristics

Parameter	Measurement
Maximum range (altitude)	327 km
Range accuracy	<6 m
Range resolution	0.312 m, least significant bit
Pulse energy	15.3 mJ at 1.064 μm
Pulse width	15 ns
Pulse frequency	1/8, 1, 2, and 8 Hz
Divergence ($1/e^2$ points)	235 μrad
Shots (lifetime)	∼10^9
Range returns	∼7×10^6
Effective RX aperture, f/#	7.62 cm, f/3.4
Optical receiver FOV	2900 μrad
Threshold levels	16 m V $\times$ 2^n, for $n = 0, 1, \ldots, 7$,
Data rates	102, 51, and 6.4 bps
Boresight relative to MSI	Line 220 $\pm$ 2; sample 260 $\pm$ 2 in rectified 412 $\times$ 537 format

Accurate morphometry of craters on Eros can help elucidate the mechanisms of crater growth: Is this growth limited by gravity of the asteroid or by material resistance to flow ("strength")? The surface of Eros has a low thermal inertia indicative of regolith cover (e.g., Harris 1998). If this regolith is deep enough, gravity-controlled cratering would be expected for most craters on Eros (e.g., Asphaug *et al.* 1996). Alternatively, for most observable crater sizes on Eros, down to a few tens of meters diameter, a "fracture-controlled" regime, intermediate between the gravity and strength regimes, may apply (Nolan *et al.* 1996). A related fundamental question, which can be addressed from profiles of steep slopes and evidence of mass wasting, relates to the depth of the regolith at Eros: How much regolith can Eros retain, given its small escape velocity of 3 to 17 m/s (varying over the surface of Eros; Yeomans *et al.* 2000). A maximum depth on the order of 100 m has been suggested based upon global mass properties of Eros assuming that the interior is minimally fractured (Zuber *et al.* 2000).

2. OBSERVATIONS

The NEAR Shoemaker spacecraft entered orbit around 433 Eros on February 14, 2000. A brief summary of the orbital mission as flown through January 2001 is given here, to provide information needed to understand the observations. The orbital coverage did not accumulate in a simple manner, and significant changes were made from plans published previously.

The spacecraft has fixed solar panels, fixed antennas, and fixed instruments (except that the NEAR infrared spectrometer has a scan mirror). The spacecraft orbital plane is constrained so that the orbit normal points to within 30° of the Sun nearly all of the time to maintain adequate power. In this orbit, the spacecraft rolls slowly to point all the instruments at Eros during data acquisition. The spacecraft points its high-gain antenna at Earth for data transmission, during which time no data are acquired because the instruments are not pointed at the asteroid. During a typical day, the spacecraft acquires data for about 16 h and transmits data to Earth for about 8 h.

Since the orbital orientation is constrained relative to the Sun, the orbital inclination relative to the equator of Eros must change throughout the rendezvous year, as Eros revolves around the Sun. The fuel expenditure and maneuver frequency required to maintain low-altitude orbits depend strongly on this inclination. Retrograde, nearly equatorial orbits at low inclination are feasible for NEAR down to orbit radii of 35 km, whereas higher inclination or prograde orbits are not feasible at such low altitudes (e.g., Scheeres 1995). The orbital history of NEAR, determined from a complicated trade-off between operational and science requirements, is summarized in Fig. 1. Orbital radii are measured from the Eros center of mass. Inclination is measured relative to the asteroid mean equator (Yeomans *et al.* 2000, Zuber *et al.* 2000).

Figure 1 shows that after orbit injection on d045 (day 45, or February 14, 2000), the spacecraft reached an apoapsis of 365 km from Eros and was injected into a nearly circular 204 × 200 km, prograde orbit on d063, at a moderate inclination of 38°. Inclinations <90° are prograde, and inclinations >90° are retrograde. The spacecraft remained in this survey orbit until d093, when it was injected into a 210 × 100 km transfer orbit to lower altitude. In the nominal 200-km survey orbit, the spacecraft completed almost three revolutions around Eros, as can be seen from the oscillations in the radius curve (reflecting the small eccentricity of the orbit). Similarly, the descent of the spacecraft can be followed from the ~200-km orbit to successively lower mapping orbits at ~100 km, ~50 km, and then ~35 km, which was attained by d196. Throughout this time the inclination generally increased as Eros revolved around the Sun. Subsequently, on d206 the spacecraft returned to higher altitude orbits, except for a low-altitude flyby to within 6.4 km of the surface on d300. The spacecraft returned to 35-km orbit on d348 and remained at low altitude thereafter.

Table II lists orbital maneuvers through November 2000 as well as the date that a new instrument software version was implemented (Cheng *et al.* 2000), causing a change in the NLR data format. Figure 1 shows when data were obtained in low orbits. The absolute accuracy of NLR range measurements improves as the range to the surface decreases (Cheng *et al.* 2000; also see Section 3), as do the probability of detection and the fraction of noise returns. NLR was designed to operate at ranges <50 km, but the first detection of Eros by NLR occurred on d060 at 290-km range. The present work uses mainly data obtained at 100-km range or less, where the single-shot probability of detection was ≫99% and the fraction of noise returns is <0.1%.

Much of the NLR data are acquired while nadir-pointed, which means pointed at the Eros center, or while offset by a few degrees (measured at the spacecraft) from nadir. The inclinations shown in Fig. 1 give the range of asteroid latitudes covered by a nadir-pointed instrument—e.g., roughly between +59° and −59° in the first 100-km orbit. For most of the time spent at 50 km or lower through d206, the spacecraft was in a polar orbit near 90° inclination, where it covered all asteroid latitudes. For the early part of the randezvous, the Sun was in the northern hemisphere of Eros, and the south pole was in shadow. Hence, although NLR covered the entire asteroid after d121, the extreme southern latitudes could not be imaged until a few months later in the mission. The subsolar point crossed the Eros equator early on d178 and remained in the southern hemisphere for the remainder of the mission.

3. SHAPE AND TOPOGRAPHY FROM NLR

NLR measures the range to the surface of Eros versus mission elapsed time (MET, as kept by the spacecraft clock). This information is converted into a shape measurement of Eros using the location of the spacecraft versus MET relative to Eros body-fixed coordinates (Eros latitude and longitude) in addition to accurate knowledge of the spacecraft pointing and instrument boresight.

TABLE II
NEAR Shoemaker Flight Events

Flight events	UTC & DOY	Date	Notes
OCM-1	1700UTC 055DOY	2/24/00	Transfer to 365 × 204 km orbit
First NLR detection	0010UTC 060DOY	2/29/00	Range 290 km
OCM-2	1800UTC 063DOY	3/3/00	Circularize at 204 × 200 km orbit
OCM-3	0203UTC 093DOY	4/2/00	Transfer to 210 × 100 km orbit
OCM-4	2120UTC 102DOY	4/11/00	Circularize at 101 × 99 km orbit
OCM-5	1522UTC 113DOY	4/22/00	Transfer to 101 × 50 km orbit
OCM-6	1531UTC 121DOY	4/30/00	Circularize at 51 × 49 km orbit
Implemented	1500UTC 174DOY	6/22/00	New NLR software and data format
NLR version 7			
OCM-7	1800UTC 189DOY	7/7/00	Transfer to 50 × 35 km orbit
OCM-8	0444UTC 196DOY	7/14/00	Circularize at 39 × 35 km orbit
OCM-9	1700UTC 206DOY	7/24/00	Transfer to 50 × 37 km orbit
OCM-10	2000UTC 213DOY	7/31/00	Circularize at 51 × 49 km orbit
OCM-11	2325UTC 221DOY	8/8/00	Inclination change at 51 km
OCM-12	2325UTC 239DOY	8/26/00	Transfer to 51 × 100 km orbit
OCM-13	2300UTC 249DOY	9/5/00	Circularize at 101 × 99 km orbit
OCM-14	0545UTC 287DOY	10/13/00	Transfer to 96 × 50 km orbit
OCM-15	2140UTC 294DOY	10/20/00	Circularize at 51 × 49 km orbit
OCM-16	2210UTC 299DOY	10/25/00	Transfer to 50 × 21 km orbit for low-altitude flyover
OCM-17	1740UTC 300DOY	10/26/00	Transfer to 61 × 200 km orbit
OCM-18	0300UTC 308DOY	11/03/00	Circularize at 198 × 196 km orbit
OCM-19	1520UTC 342DOY	12/07/00	Transfer to 196 × 35 km orbit
OCM-20	2015UTC 348DOY	12/13/00	Circularize at 36 × 34 km orbit
OCM-21	1605UTC 024DOY	1/24/01	Transfer to 35 × 24 km orbit
OCM-22	0125UTC 028DOY	1/28/01	Transfer to 36 × 19 km orbit
OCM-23	1805UTC 028DOY	1/28/01	Transfer to 35 × 37 km orbit

Notes. OCM, orbital correction maneuver; UTC, coordinated universal time; DOY, day of year.
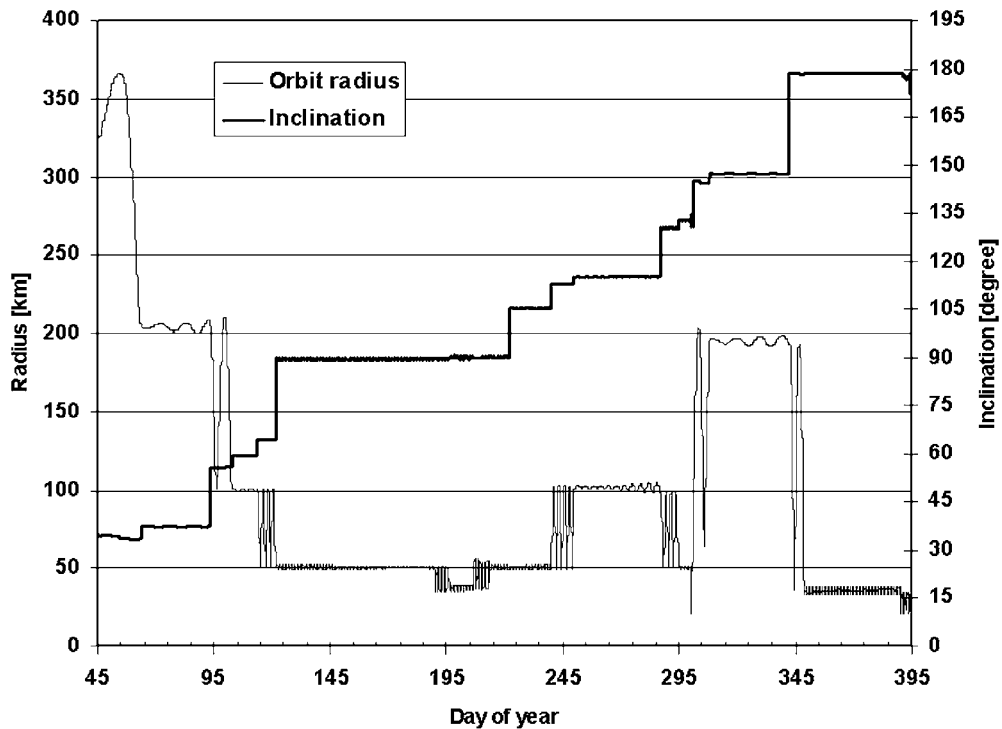

FIG. 1. Mission timeline as flown through January 2001. The orbit radius (left axis) and orbit inclination relative to the Eros equator (right axis) are plotted versus day of year 2000, beginning at orbit injection on February 14, 2000.

The highly irregular shape of Eros requires a *simultaneous* solution for the spacecraft ephemeris, the asteroid shape, the asteroid rotation state, and the gravity field (Zuber *et al.* 1997, Yeomans *et al.* 1997). Unlike the case with previous investigations of Mars, the Moon, and the Earth, the spacecraft ephemeris cannot be determined with sufficient accuracy (even for navigation) from radiometric data alone. Even for the Moon and Mars, gravity and altimetry studies find that joint inversions for gravity and topography significantly improve the solutions for both (Smith *et al.* 1999, 2000, Zuber *et al.* 1994).

At present it is difficult to quantify how well laser spots can be absolutely located in asteroid body-fixed coordinates. Although individual laser measurements have a range precision of about 1 m from 40-km range (Cheng *et al.* 2000), absolute topography cannot yet be determined to this accuracy. Currently, the rms error in the spacecraft ephemeris, as estimated by the scatter of the solution points, is about 30 m (Zuber *et al.* 2000, Yeomans *et al.* 2000), but these errors are nonuniform and nonrandomly distributed.

This paper emphasizes results obtained from *relative* topography of small-scale features, using contiguous altimetric profiles of 2000-s typical length. Over such a short time span, the ephemeris error introduces primarily an overall positional bias to the altimetric track which does not change appreciably over the course of the track. Additional sources of error in the relative topography arise from uncertainties in spacecraft timing and spacecraft pointing. From analyses of gamma ray burst data from the NEAR gamma ray spectrometer, the absolute timing of NEAR spacecraft events is known to within 20 ms (D. Tillman, private communication, 1999). Given the typical spacecraft orbital velocities of <5 m/s, absolute timing uncertainties are completely negligible for NLR topographic analyses. The typical uncertainty in absolute pointing of the NEAR spacecraft, during NLR data acquisition, is estimated as 100 μrad, degrading significantly during rapid slews (it is more uncertain for faster slews). This pointing uncertainty arises from the presence of an irregular, three-axis spacecraft oscillation with a variable period on the order of a minute, whose amplitude is less than but comparable to the laser beamwidth of 235 μrad (Table I). The spacecraft achieves better pointing accuracy, typically <40 μrad, for optical navigation using stars with fixed inertial pointing (during data acquisition at Eros, the spacecraft must execute a continuous slew to keep the instruments pointed at the asteroid). The data analyzed here are selected for absence of rapid slews. With a pointing uncertainty estimated as 100 μrad, the position error normal to the boresight is about 4 m at a range of 40 km. The incidence angles on the surface (relative to the local surface normal) are often large (i.e., >45°) and are typically unknown on the spatial scale of the laser footprint. Hence, an absolute range error results from pointing uncertainty. In addition, pulse dilation arises from the finite laser-beamwidth (pulse dilation is the temporal stretching of the return pulse when different parts of the laser-illuminated target area differ in their ranges from NLR; e.g., see Cheng *et al.* 2000). Pulse dilation results both from nonnormal incidence and from surface roughness. Both pulse dilation and pointing uncertainty contribute to the total uncertainty in the absolute range, about 5 m at 40-km range. Both contributions to the absolute ranging uncertainty are directly proportional to the range to the surface, so that more accurate ranges are measured in the lower orbits.

However, the present work focuses on the relative topography and not the absolute radius of small-scale features. The uncertainty in the relative topography can be estimated from the scatter in the ranging measurements and is on the order of a meter (see Section 4). Even with the relative surface heights measured to within a meter along the track defined by successive laser footprints, individual altimetric profiles can be difficult to interpret: A dip in elevation may be a central track through a small crater, an off-center track through a much larger crater, or a track through a groove. For a groove, the width cannot be determined without knowing the orientation relative to the track. In principle, once a sufficient number of altimetric tracks is assembled into a regional DTM, these difficulties are overcome, and the geology of the site can be interpreted. However, as mentioned in Section 1 available spacecraft ephemerides do not yet support creation of high-resolution DTMs.

The present work uses an alternative approach to the interpretation of small-scale topographic profiles, which is to co-register the profiles with simultaneous images of the same region. Co-registered images complement the topographic data, with each enhancing the interpretation of the other. Altimetric data, for instance, allow separation of brightness variations due to topography from those due to albedo. Images distinguish, for example, craters from grooves. The NLR and MSI teams pursued two approaches to co-registration of NLR profiles with MSI data: (i) direct attempts to image the NLR laser spot with MSI under special conditions and (ii) correlation of simultaneous MSI and NLR data. Because MSI is limited to exposures of <1 s, attempts to detect the NLR spot were not successful.

4. BORESIGHT ALIGNMENT OF NLR AND MSI

The current best estimate for the NLR boresight location relative to the MSI FOV, in line-and-sample pixel coordinates, is given in Table I. These coordinates are defined for the *rectified* pixel format, in which an MSI frame has 412 lines and 537 samples. When the image is displayed as in this paper, the first line (line number 0) is at the top, and the first sample is at the left. Each pixel in the rectified format is square and subtends 95.9 μrad. The NLR laser beamwidth is 235 μrad full width (2.45 image pixels). MSI images are actually acquired in a 244 × 537 format with rectangular pixels, and the rectification is accomplished in postprocessing (Murchie *et al.* 1999).

The boresight alignments of NEAR instruments were measured prior to launch (Cheng *et al.* 1997), but images of star fields have revealed postlaunch changes in the MSI alignment relative to the spacecraft inertial reference system prior to NEAR's arrival at Eros (Murchie *et al.* 1999). It was not possible to monitor

postlaunch changes in the NLR alignment until arrival at Eros, but changes were expected because of launch stresses and continually changing thermal environments experienced during cruise. Once in orbit around Eros, the instruments have been maintained in a relatively stable thermal environment, because solar illumination must be maintained on fixed solar panels and the instruments are always in shadow. The instruments have not been subjected to significant vibration (the spacecraft attitude is controlled by reaction wheels). The data analyzed in this paper do not indicate shifts in the NLR boresight alignment relative to MSI.

The following procedure was used to determine the NLR boresight relative to the MSI FOV. The first step was to constrain the laser boresight location to as small a fraction of the MSI FOV as possible before attempting detailed correlations between altitude profiles and images. This procedure was necessary because of the extreme irregularity of Eros's shape. The problem at Eros is unlike that of much larger bodies where relatively flat areas can be found with large, isolated topographic features (e.g., craters or volcanoes) that can be identified readily and unambiguously in both images and altitude profiles (Smith *et al.* 1997)—there are no such areas on Eros. A multiplicity of topographic features at all detectable scales is evident both in images and in altitude profiles, and the task of finding correlations among them, without substantial prior knowledge of where to look in the images, seemed extremely daunting.

A new approach was therefore required to correlate images and altitude profiles from an extremely irregular small body, with imprecise prior knowledge of the boresight alignments. The task was, essentially, to identify corresponding events in the images and altitude profiles that could be found easily and unambiguously. The desired type of event turned out to be limb observations. When the laser boresight drifts off the asteroid, no more laser returns are detected. More precisely, laser returns are lost as soon as the incidence angle to the surface becomes too great, because of pulse dilation, before the boresight actually reaches the visible limb. Hence the occurrence of limbs in the images could be readily correlated with dropouts in the laser returns, once the spacecraft reached a low enough orbit (100 km or lower) that laser returns are consistently detected whenever the boresight is on the asteroid.

Limb detections alone provide a useful constraint on a boresight alignment. Two examples are shown in Fig. 2. In both cases, at the times of the images (MET, measured in seconds from the start of the mission, is marked on the image) laser returns were received, indicating that the laser spot was on the asteroid at those times. Examination of numerous cases quickly demonstrates that the laser boresight is near the center of the MSI FOV, close to its prelaunch alignment.

Figure 2 combines two limb observations with an observation of the 5-km Psyche crater (centered 32°N, 95°W) from 190-km range. Psyche is the largest feature on Eros that has the characteristic morphology of an impact crater (Zuber *et al.* 2000) and is readily identified both in images and in altitude profiles.
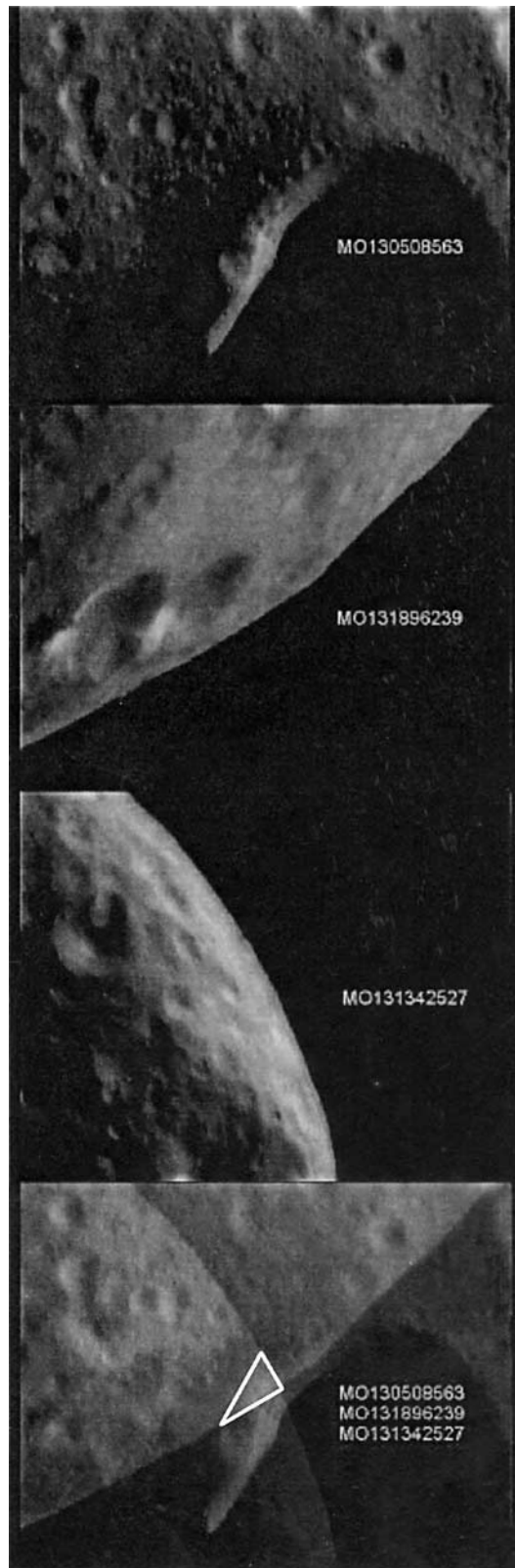

FIG. 2. Constraint of NLR boresight using a Psyche observation (top) and two limb observations at the times indicated. The boresight is constrained within the white triangle sketched in the bottom panel.

The Sun is always to the right in MSI images; when the limb cuts from top to bottom of the image frame, the asteroid is always to the left (because the *illuminated* limb is always targeted); if the only times used are those when laser returns are seen, the boresight is always constrained to the *left* of some curve. To obtain a constraint that the boresight is to the *right* of some curve, using a limb observation, a time must be selected when the boresight is off the asteroid (or too close to the limb) and no returns are received. The difficulty is that lack of a laser return implies only a high probability, but not a definite inference, that the boresight is off the limb. With a sufficient number of limb observations, the correct laser alignment was inferred with high confidence and confirmed by later observations. However, for definiteness, Fig. 2 constrains the boresight to the *right* of some curve using a Psyche observation. That is, at the time shown in the top panel of Fig. 2, the laser spot was interior to the peak of the rim of Psyche, which was crossed ~100 s later (see Fig. 3a). The top three panels of Fig. 2 are superposed in the bottom panel, constraining the laser boresight within the triangular area marked.

Figure 3 shows additional details of the Psyche observation used in Fig. 2. The NLR range profile is shown in Fig. 3a, where the three vertical lines mark the times of the three images in Figs. 3b–3d. This NLR profile is typical of data returned from the vicinity of 200 km and is instructive in regard to data quality. The image of Fig. 3c is the one used in Fig. 2. Only spotty returns are obtained from the bottom of the crater. No returns are obtained from the steep walls of Psyche, but consistent returns are seen once the laser spot has climbed out near the rim. The reason for the NLR data dropouts is pulse dilation, from oblique incidence and from surface roughness, which stretches out the return pulses in time to an extent that they are no longer detected. At 190-km range, the single-shot probability of detection decreases significantly, even from a smooth surface with the average reflectivity of Eros, once the incidence angle exceeds $35°$ (Cheng *et al*. 2000). Even with nadir pointing, such large incidence angles are common given the irregular shape of the asteroid (Zuber *et al*. 2000).

NLR was designed to operate at 50 km (Cole *et al*. 1997). The data returned from ~200 km are of great value for determining global shape and mass properties (Zuber *et al*. 2000), but the small-scale topography results discussed below rely on data from ~100 km or lower. In these latter orbits, data dropouts caused by pulse dilation are negligible.

Once the laser boresight was constrained near the center of the MSI FOV, it became possible to make detailed correlations between NLR profiles and MSI images. Figures 4 and 5 show two examples of times when the NLR profile detected a block very close to when an image was obtained. These instances provide relatively precise constraints on the location of the NLR boresight. Figure 4 shows an image obtained on d117 at a range of 47 km from the surface at $224°E$, $17°S$, located west of Psyche crater. The crosshairs in the image are centered at (sample 260, line 220) and mark a feature that can also be seen in the
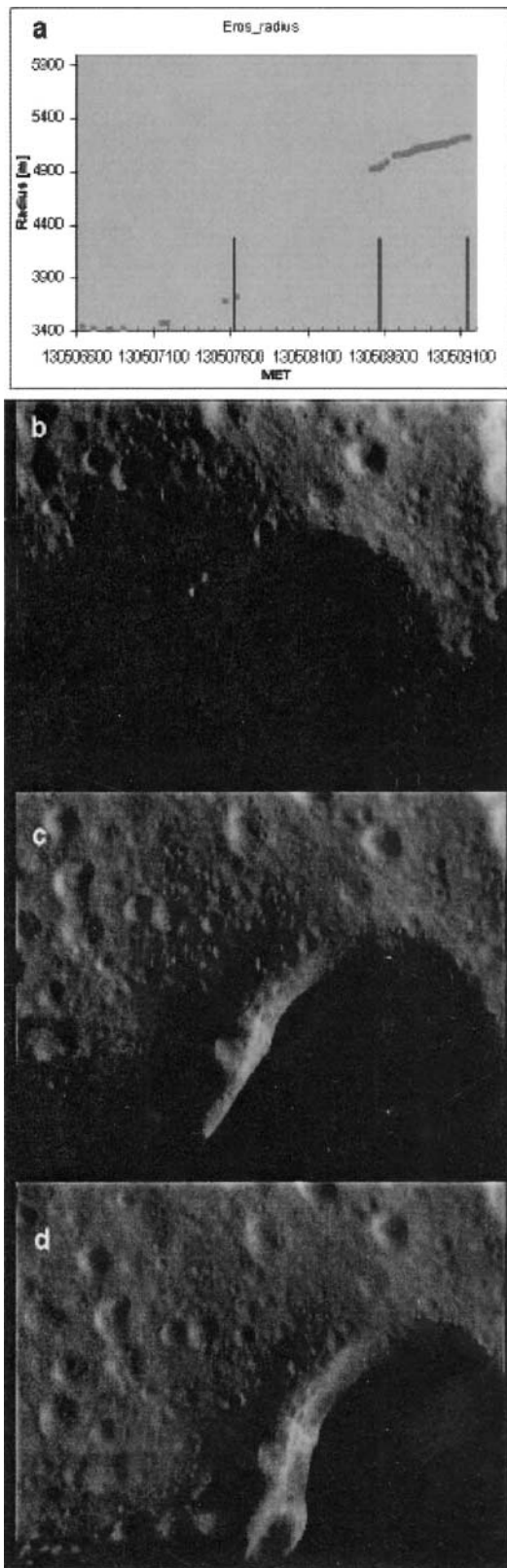

FIG. 3. Detail of Psyche observation in Fig. 2. The vertical lines in the top panel mark the times at which the images in the lower three panels were obtained.

accompanying NLR profile (upper panel), where the vertical line marks the time of the image. The block in this case is a ~12-m feature. There are four laser shots, from MET 132123649.5 to 132123652.5, on top of the block. The image was acquired 3 s later, at MET 132123655 (the image is exposed toward the end of the 1-s major frame; Cheng *et al.*, 2000). The average angular rate at which the surface moved past the boresight was 39 μrad s^{-1} during this event, or about 1 pixel in 3 s. Specifically, if the boresight spot is the (vector) $\mathbf{x}_1$ at time t_1 but is the point $\mathbf{x}_2$ at time t_2, and if the ranges measured are r_1 and r_2, respectively, at these times, then the average angular rate is given by

$$ rate = \frac{2\sqrt{(\mathbf{x}_1 - \mathbf{x}_2)^2 - (r_1 - r_2)^2}}{(r_1 + r_2)(t_2 - t_1)}. \tag{1} $$

The angular rate is due to a combination of asteroid rotation, spacecraft orbital motion, and slew. The 95.9-μrad rectified MSI pixel subtends 4.5 m at 47 km.

In Figure 4, a linear trend is subtracted from the radius curve, and the residual is plotted as "detrended radius," in which the block stands out dramatically. The precision of the range measurements is on the order of a meter, as can be judged from the scatter in the detrended radius points.

Figure 5 shows a similar observation from d125 at a range of 42 km, in a boulder-rich area at 26.6°E, 13.6°S on the opposite side of Eros from the area in Fig. 4. The crosshairs on the image mark the same pixel coordinates (sample 260, line 220). A tall boulder can be seen at (262, 218) with its shadow extending to the lower left. The detrended radius profile reveals a 30-m spike, marked with a vertical line in the plot, comprising 20 laser shots from peak to trough. The peak radius was measured by NLR at MET 132836811.5, which was 7 s before the time of the image. During this 7-s interval, the average angular rate of the surface was 56 μrad s^{-1}. After correction for 7 s of angular motion, the NLR boresight is inferred to be within 1 pixel of (sample 260, line 220). The 95.9 μrad rectified MSI pixel corresponds to 4 m at a range of 42 km.

In summary, instances like those in Figs. 4 and 5 provide a boresight determination within a ±2 pixel uncertainty. To date, numerous instances have been analyzed, including cases of topographic overhangs (not shown) which are observed as sudden jumps in radius. The resulting estimate of the boresight alignment is given in Table I.

It is remarkable that blocks can be identified in NLR profiles that sample only a small fraction of the surface area. This testifies to the high surface abundance of blocks at Eros (Veverka *et al.* 2000). The NLR profiles in Figs. 4 and 5 appear rough but need to be interpreted with caution. This is because the irregular shape of Eros implies that radius, meaning distance to the center, is not a satisfactory measure of elevation. Likewise, the mission elapsed time does not measure horizontal distance even if the slew rate of the boresight is nearly constant (as it is in Figs. 4 and 5), but displacement perpendicular to

the boresight must be projected onto the surface. By plotting radius versus mission time, Figs. 4 and 5 avoid these complications.

5. DEFINITION OF ELEVATION ON IRREGULAR OBJECTS

The geophysically significant measure of elevation is the height relative to the geoid, meaning the local equipotential surface, where potential now means the combined gravitational and centrifugal potential (or "geopotential") for an object resting on the surface. If a small plumb bob hangs near the surface of an irregular body, the geoid is locally perpendicular to the plumb bob. The geoid is the reference surface to which local slopes are measured, and uphill directions are those in which the geopotential increases. The geopotential is given by

$$ \Phi(\mathbf{x}) = -\int d^3\mathbf{x}' \frac{G\rho}{|\mathbf{x} - \mathbf{x}'|} - \frac{\Omega^2 r^2}{2}, \tag{2} $$

where the gravitational potential at $\mathbf{x}$ is found from an integral over the volume of the asteroid, r is the distance from the point $\mathbf{x}$ to the rotation axis, Ω is the rotation rate of 3.31166×10^{-4} rad s^{-1} (Zuber *et al.* 2000, Yeomans *et al.* 2000), G is the gravitation constant, and ρ is the density.

An NLR profile consists of a sequence of points $\mathbf{x}_i$ at which the elevations are required. To trace a reference geoid surface through one of these points, and then to measure the distance to this reference geoid for each data sample $\mathbf{x}_i$, is a rigorous but computationally expensive procedure. A much simpler approximation is to define a *relative* geopotential height h as

$$ h(\mathbf{x}_i) = |\Phi(\mathbf{x}_i)/g_{avg}|. \tag{3} $$

That is, $h(\mathbf{x})$ measured in meters is proportional to geopotential itself but is scaled by a factor g_{avg}, which is the local average magnitude of the acceleration of (effective) gravity. The approximation involved in using $h(\mathbf{x})$ is essentially the neglect of the variation in gravitational acceleration over a short altitude profile, which is an excellent approximation (within a meter, or comparable to the measurement precision). Also, $h(\mathbf{x})$ is a relative height. In what follows, an arbitrary reference height is subtracted from $h(\mathbf{x})$.

The NLR profiles are reduced to determine relative geopotential height according to (3). This procedure requires calculating the integral in (2) at every NLR data sample in the profile, as well as finding the value of g_{avg} from another similar calculation. These calculations use a shape model for the asteroid and assume a constant density (corresponding to a total mass of 6.687×10^{18} gr; Yeomans *et al.* 2000). The surface potentials and gravity are calculated from the shape model, rather than from the gravitational harmonics inferred from radio tracking of the spacecraft (Yeomans *et al.* 2000, Zuber *et al.* 2000). Because the spherical harmonic expansion is valid outside a sphere containing
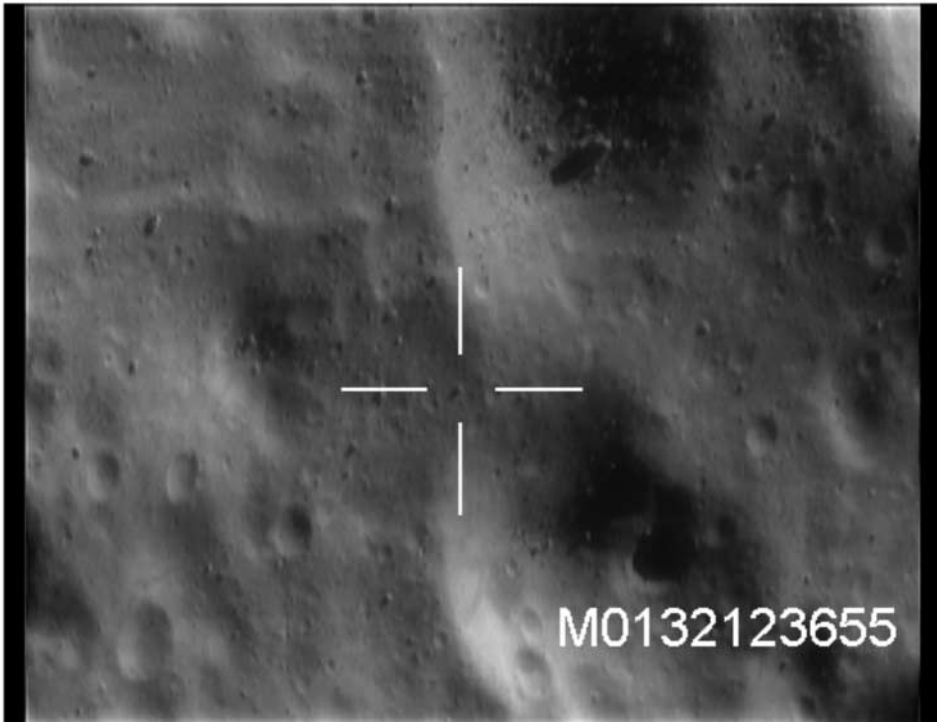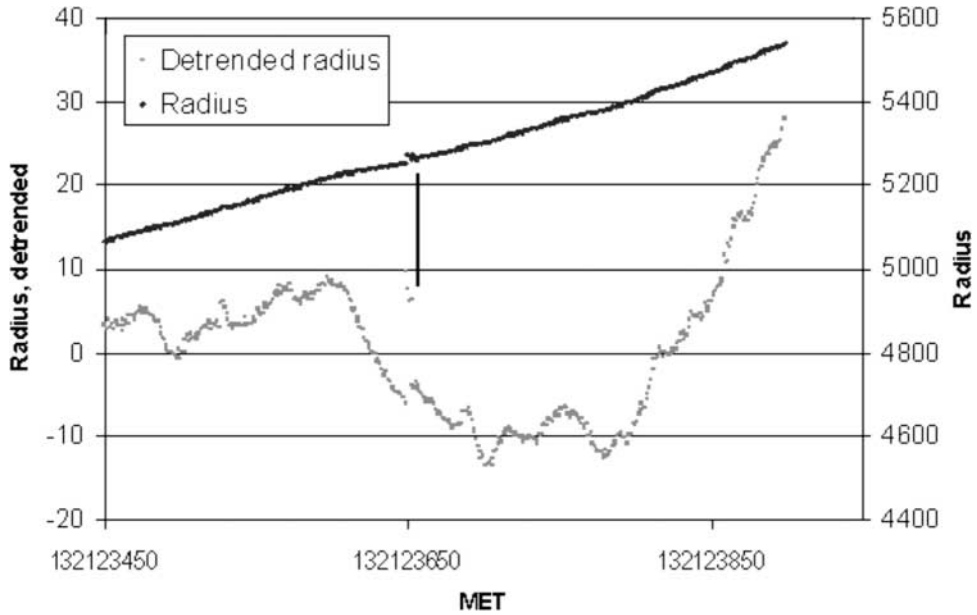
FIG. 4. Constraint of NLR boresight with observation of a boulder. The upper panel plots Eros's radius (right axis) and detrended radius (left axis). The vertical line marks the time of the image in the lower panel. The crosshairs drawn on the image mark the pixel at line = 220, sample = 260.

all the mass of Eros, it breaks down on or close to the surface of Eros. In addition, the short-wavelength structure of the gravity field is of interest for the present work. Comparison of the measured gravitational harmonics from radio tracking with harmonics calculated from the shape model shows that the density is approximately uniform within the volume of Eros (Yeomans *et al*. 2000, Zuber *et al*. 2000).

The Appendix outlines a computationally efficient means of performing these calculations using shape models for Eros that tessellate the surface with triangles. This shape model and associated data structures will be referred to as the "plate model." It is the standard Eros shape model used for spacecraft operations by the NEAR Project and is supported by the JPL SPICE data system. The plate model is described in the Appendix as it is not
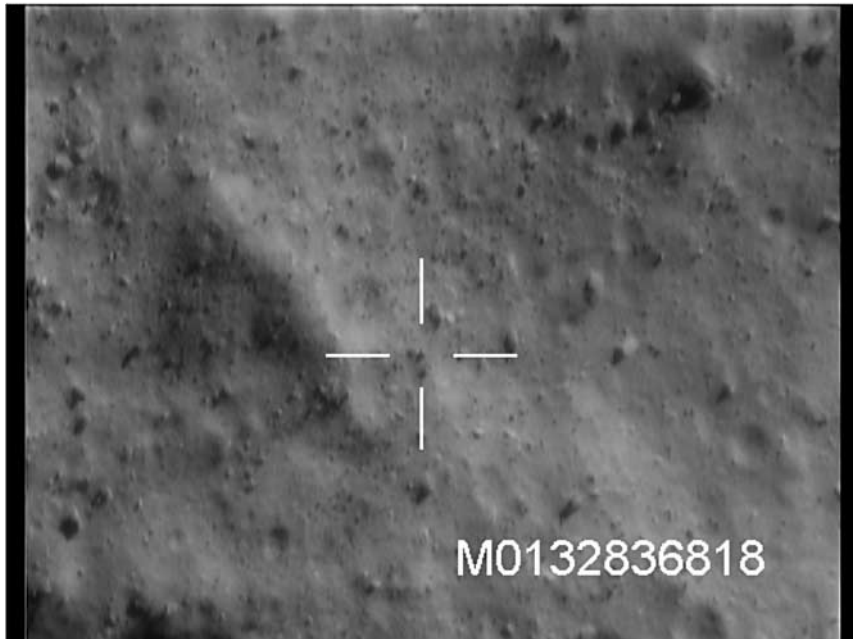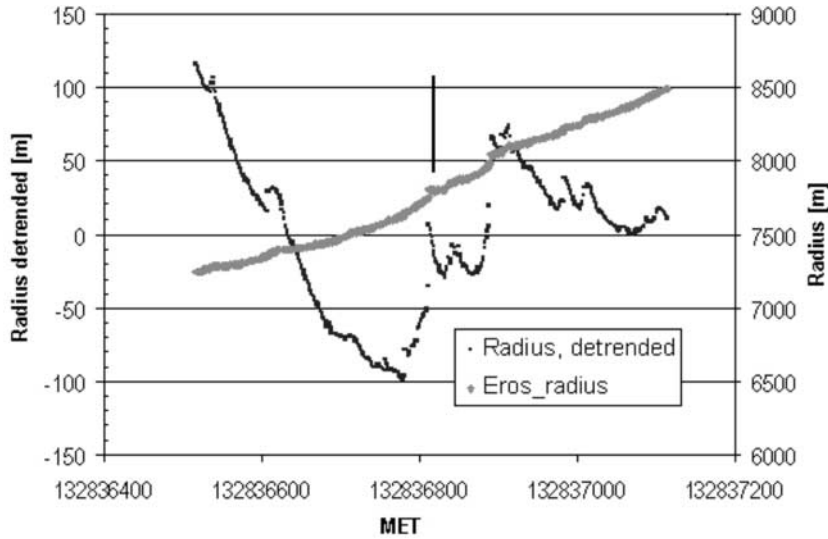
FIG. 5.   Same as Fig. 4 but for a different boulder.

documented elsewhere. The version called NLR190 is used for the analyses reported here (Zuber *et al*. 2000).

Figure 6 illustrates the determination of geopotential height. NLR data from d117 are shown with an MSI image (cropped) that was taken at MET 132124684 and at a range from the surface of 46 km. The crater is located at 211°E, 17°S. The NLR track is off-center, and so the measured depth is less than the maximum depth of the crater. Three methods are shown for finding "height" from NLR range data. The first is detrended radius, or distance to the center of Eros with a linear trend subtracted. The detrended radius shows the greatest topographic contrast, or depth of the crater relative to its diameter. The detrended radius curve would imply that this crater had a depth-to-diameter

ratio of 0.26, which is larger than observed for fresh craters on the Moon or in laboratory experiments. The depth found from detrended radius would not be consistent with an impact origin for the feature. However, if the detrended radius curve is simply projected in the direction of the local surface normal (determined from the NLR190 shape model; Zuber *et al*. 2000), then the topographic contrast is reduced by a factor of 1.3, as shown in the curve labeled "geometric height." The third measure is the geopotential height from (3) with an arbitrary zero at the initial MET, which gives a topographic contrast similar to that from geometric height. The geopotential yields a depth-to-diameter ratio of 0.13, which is consistent with values observed for small impact craters on the Moon. Thomas *et al*. (1996) have
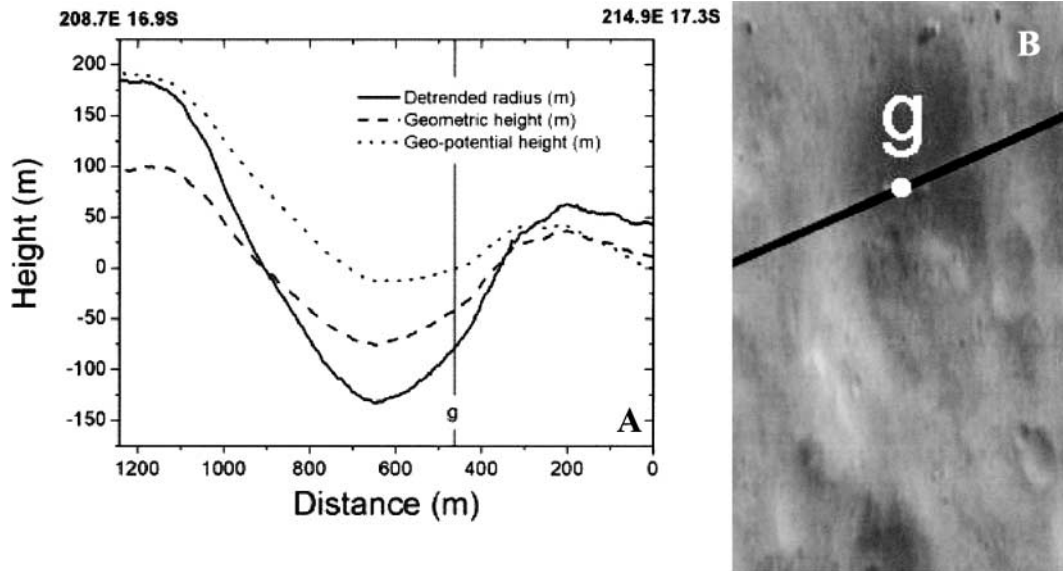
FIG. 6. Three measures of height compared for a crater at 211°E, 17°S. The detrended radius overestimates the topography, and the geometric height (detrended radius projected to outward normal) underestimates it.

previously noted that geopotential height tends to subdue the topographic contrast when compared to radius from the center. In what follows, only geopotential height will be used to measure topography.

The geopotential height in Fig. 6 and in subsequent figures is plotted versus "distance" determined by fitting the NLR track in three dimensions to a line. Individual laser spots are projected onto this best-fit line, and "distance" is measured along this line. The process is analogous to laying a meter stick along a short track and reading off the distances. Because this distance is not measured at constant elevation, slope is not simply related to the graphical slope of the geopotential curves as in Fig. 6. Slope is determined from the geopotential height difference and the magnitude of the displacement vector between two points.

6. TOPOGRAPHY OF SURFACE FEATURES ON EROS

This section presents examples of the diverse topographic features seen on Eros. NLR topographic profiles with boresighted MSI images provide evidence for benched craters, square or jointed craters, mass wasting, and structural features. The extreme roughness of Eros's surface is characterized by calculating fractal dimensions.

Downslope motion in craters. Figures 7–9 present observations of two craters with evidence of downslope motion. The crater in Fig. 7 is located between 257°E, 14°S and 264°E, 13°S, west of Psyche. These are the endpoints of the NLR profile shown in Fig. 7A. The inset to Fig. 7A is an MSI image (cropped) taken during the NLR profile on d117. The curve shown is the geopotential height from (3) versus distance defined above. The crater diameter (rim to rim), measured according to distance from the point a to the last of the three ridges marked in Fig. 7A,

is 342 m. The depths, measured as the maximum difference in geopotential between the profile and a line drawn from rim to rim, is about 45 m for a depth/diameter ~0.13. The crater formed on a 19° slope measured along the profile.

Figures 7B and 7C use a different MSI image (cropped) taken on d135, under similar lighting conditions. North is approximately upward in the images. The NLR track is drawn as the white line in the inset d117 image and is drawn through the corresponding features in the d135 image as the black lines in Figs. 7B and 7C. The points a–d in Fig. 7A are marked in Fig. 7B according to distance along the track; the slope changes at points a–d are seen to correspond to bright and dark linear features in the southwest wall of the crater as imaged on both d117 and d135. The solid white curve drawn in Fig. 7C at the left of the track marks the brightness change at point d.

The darker material toward the northeast side of the crater is interpreted as an accumulation of unconsolidated debris that has slid down the steep slopes found in a–d. The boundary of the dark material in the slide is marked as dots in the sketch of Fig. 7C. The steepest slopes along the profiles shown in Fig. 7A are 57° and 51°. The slope measured along the track is a lower limit to the slope of steepest descent, but the latter is not determined because a high-resolution digital terrain model is not available. The slope at the front of the slide is comparable to the average slope of 19° along the entire track. These data are consistent with occurrence of a landslide, meaning a rapid, coherent downslope motion resulting from slope failure in a well-defined region, most likely the steep slopes in segment a–d. For a small body such as Eros, the free-fall time is increased relative to that on large bodies by the inverse square root of the surface gravity, so any landslide would have reduced "rapidity" compared to that on a large body.
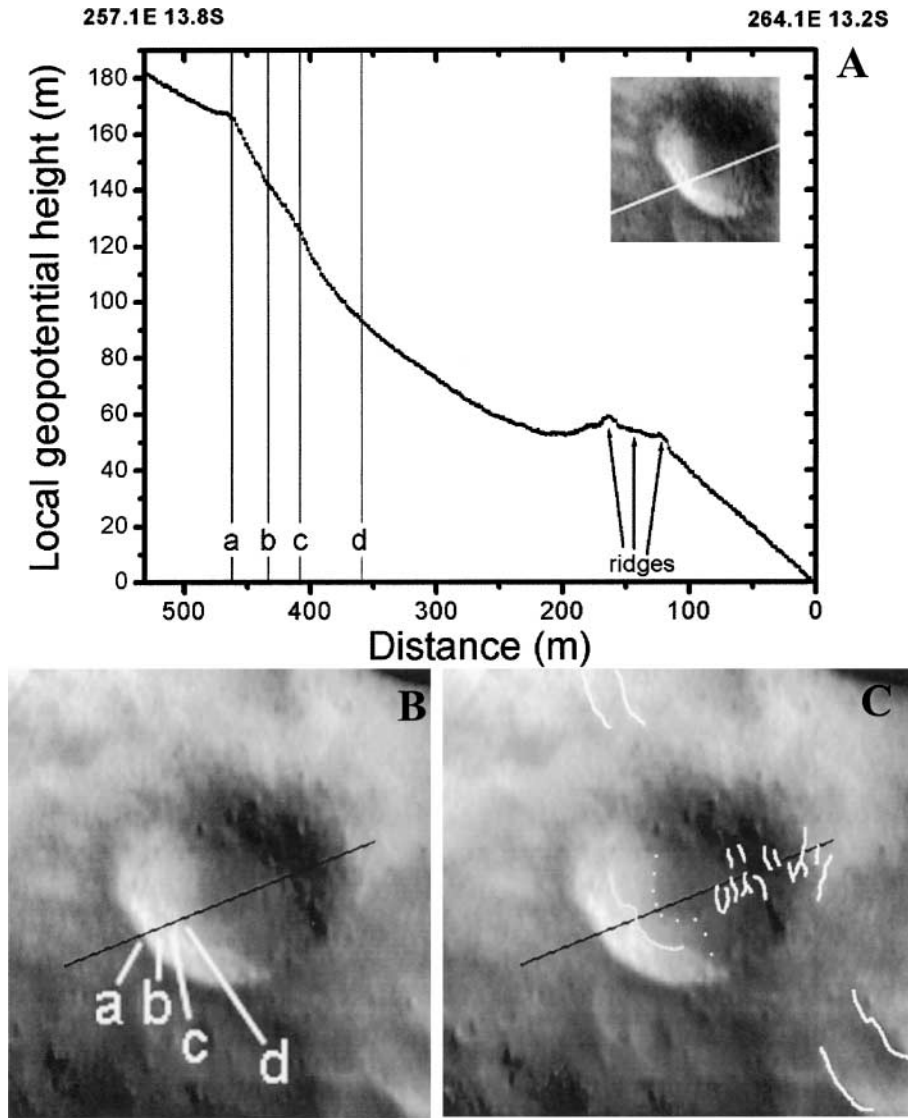
FIG. 7. Mass wasting in a crater west of Psyche. The geopotential height profile is plotted in panel (A), where the inset image was taken at MET132122584 and at 48-km range. The track is drawn on panels (B) and (C), where points a through d are marked corresponding to the times in panel (A). Longitude and latitude are shown for the start point and the end point of the track. Panels (B) and (C) show an image taken at MET 133697418 and at 46-km range. The sketch in panel (C) marks a possible bench, slide material, and small tectonic ridges.

Another possible interpretation of the slope changes in segment a–d is that they indicate formation of a bench during crater excavation, when relatively unconsolidated material on the surface of Eros excavated more easily than a more consolidated, deeper layer. The darker band between points b and c corresponds to a shallower slope in the height profile, as compared with the steeper slopes in a–b and c–d. The thickness of the unconsolidated upper layer is estimated from the depth of the shallow slope feature b–c, which is ~20 m relative to the pre-impact surface. The formation of crater benches has been documented in the laboratory when the diameter of the crater is more than 10 times the depth of the bench, as in the present case. Crater benches have been used to determine the thickness of regolith on

the Moon (Quaide and Oberbeck 1968). If a bench is present in the crater of Fig. 7, the downslope motion discussed above may have occurred in the late-stage crater modification associated with collapse of the transient cavity (e.g., Melosh 1989). This crater formed in a significant regional slope of 19°, which may have caused the modification to take the form of mass movement across the crater in the downslope direction. The steep slopes found in segments c–d and a–b indicate where slope failures likely occurred to trigger this mass movement.

The NLR profile also reveals positive relief features that can be identified in the images as small ridges on the northeast (lower elevation) side of the crater, marked as white linear segments in Fig. 7C. These positive relief features are a few meters in height
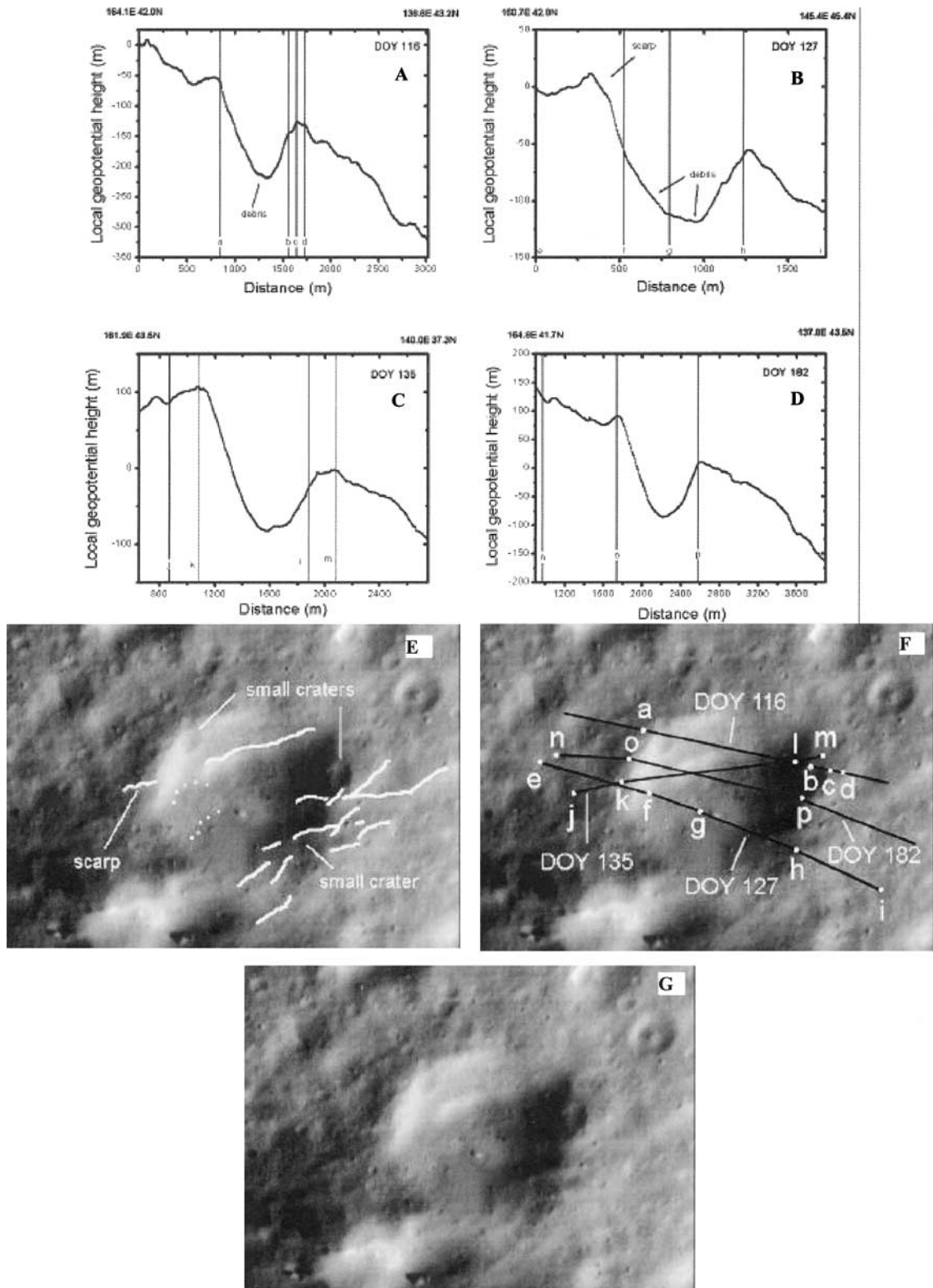
FIG. 8. Mass wasting in a crater northeast of Himeros. The four NLR profiles in panels (A)–(D), are in the same format as in Fig. 7. The image in panels (E)–(G) was taken at MET 133010313 on d127 at a range of 43 km. In panel (E), the scarp called out in profile (B) is marked, and linear structural features are sketched that are intersected by NLR tracks. Dots outline brighter material interpreted as a slide. Panel F shows the NLR tracks and points called out on the profiles. In panel (B), lines e and i coincide with the left and right axes, respectively.

and are associated with a system of troughs trending from the southeast to the northwest, some of which are marked in Fig. 7C. The NLR profile resolves one of these depressions at a distance of ~170 m. As these structural features appear related to similar features found outside the crater, they most likely indicate the presence of preexisting fractures.

Figure 8 shows a relatively degraded 860-m (rim-to-rim) diameter crater, circa 153°E, 42°N northeast of the large, saddle-like feature Himeros. Figures 8A–8D show NLR profiles from four different days, with a distance scale given as before, and with a different zero of height for each profile. Figures 8E–8G use a boresighted image from the observation shown in Fig. 8B on d127. The NLR profiles encountered many small craters, including one seen in Fig. 8A after point a and another seen after point b. A third small crater is seen in the profile of Fig. 8B before point h, but this crater is in the wall of a groove that runs over the rim and down the wall of the 860-m crater. Structural features, such as the scarp called out in Fig. 8B, are sketched in Fig. 8E. The linear structural features in this region form at least two intersecting systems, consistent with their being associated with fractures in a consolidated substrate.

The average slope of the profile in Fig. 8A is representative of average slopes in Fig. 8 and is ~5°. In Fig. 8B, the segment f–g transects relatively bright material that has an average slope of 12°. This bright material lies immediately below a slope of 28°, the steepest in the segment e–f. These slope changes are interpreted as indicating a landslide, in which the bright material moved downslope after a slope failure above point f where the slope is even steeper (based on another NLR track, which is not shown). The blocky texture of this bright material is consistent with occurrence of a slide. The scarp marked between e and f in Fig. 8B is outside the rim of the crater.

The floor of the crater is partially filled by debris, only some of which originated in the slide. The NLR profile of Fig. 8B shows that the area encountered after point g is relatively flat; the 600- to 1000-m distances of the segment g–h in Fig. 8B have a slope close to the regional value. The flatness of the crater bottom near point g may be consistent with mantling, possibly by crater ejecta. The depth of point g relative to the crater rim from segment e–i, between the scarp and the point f at the slope change, is 107 m. The depth from point o to the bottom of the crater on segment o–p is 176 m, and the depth from point k to the bottom of the crater on segment k–l is 187 m. The overall depth of the crater, measured from the average of the two rim heights in segment o–p of Fig. 8D, is 133 m (depth/diameter ~0.14).

The brighter material transected in segment f–g is interpreted as a more recent slide superposed on previous infill. We estimate the thickness of this deposit by fitting a quadratic function to the steep crater walls seen in the NLR profile obtained on DOY 127 (Fig. 9). The fitted quadratic function models a possible crater profile before the slide. The total width w of slide material is marked in Fig. 9, as is the corresponding area A. The maximum thickness of the deposit is 15 m in this model. While the cubic
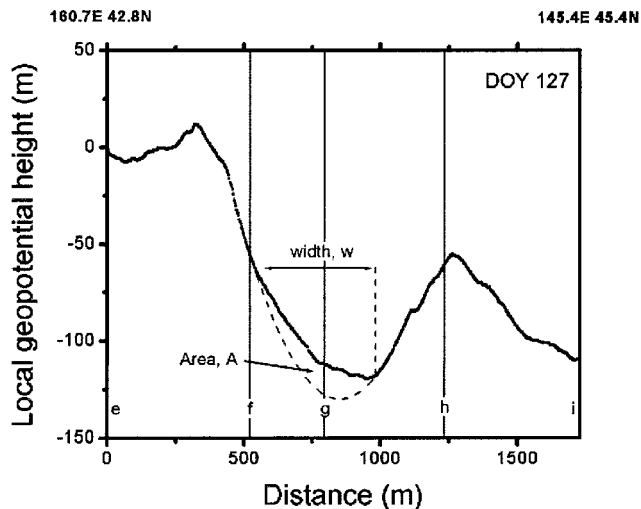

FIG. 9. The crater profile of Fig. 8B. The area A between the cubic fit and the profile models the amount of debris accumulated within the crater.

fit may be affected by the presence of the groove wall before point h, the estimated thickness is not changed qualitatively.

The crater in Fig. 8 may have a bench about 50 m below the rim. The image suggests the presence of a bench that is covered by infill in the region surrounding point g. Slope changes are seen in the profile a–b of Fig. 8A, before the features called out as "debris," that are consistent with presence of a bench. However, the slopes in the corresponding portion of segment o–p in Fig. 8D are steep, and slope changes, if present there, are subtle. The central depression in the profile k–l of Fig. 8C may be a degraded crater, rather than related to presence of a bench.

Grooves, ridges, and craters. Figure 10 shows NLR and MSI observations of a square crater, located circa 143°E, 17°S southeast of Himeros. The NLR profiles in Figs. 10A and 10B were taken on d117 and d170 respectively. Figure 10C is a boresighted image (cropped) obtained during the profile shown in Fig. 10A. The boresighted images from d170 were obtained under extremely low Sun illumination and are not shown. The mosaic (Fig. 10D) was compiled from images taken on d198. The NLR tracks are indicated on Fig. 10D by locating the corresponding features in Fig. 10C.

This square crater is interpreted as exhibiting the effect of structural control of crater formation by preexisting fracture systems in the surface, which results in formation of jointed craters. The Barringer Meteor Crater in Arizona is a famous example of a small, structurally controlled crater (e.g., Shoemaker 1963). In Meteor Crater, the regional joint trends are close to orthogonal and tend to bisect the crater, with the straight sides of the crater found at large angles to the planes of weakness. A different form of structural control is exhibited by Fig. 10, where the straight sides of the crater are almost parallel to the regional systems of ridges and grooves. The type of structural control in Fig. 10 can be caused by structural control of the rim collapse phase of
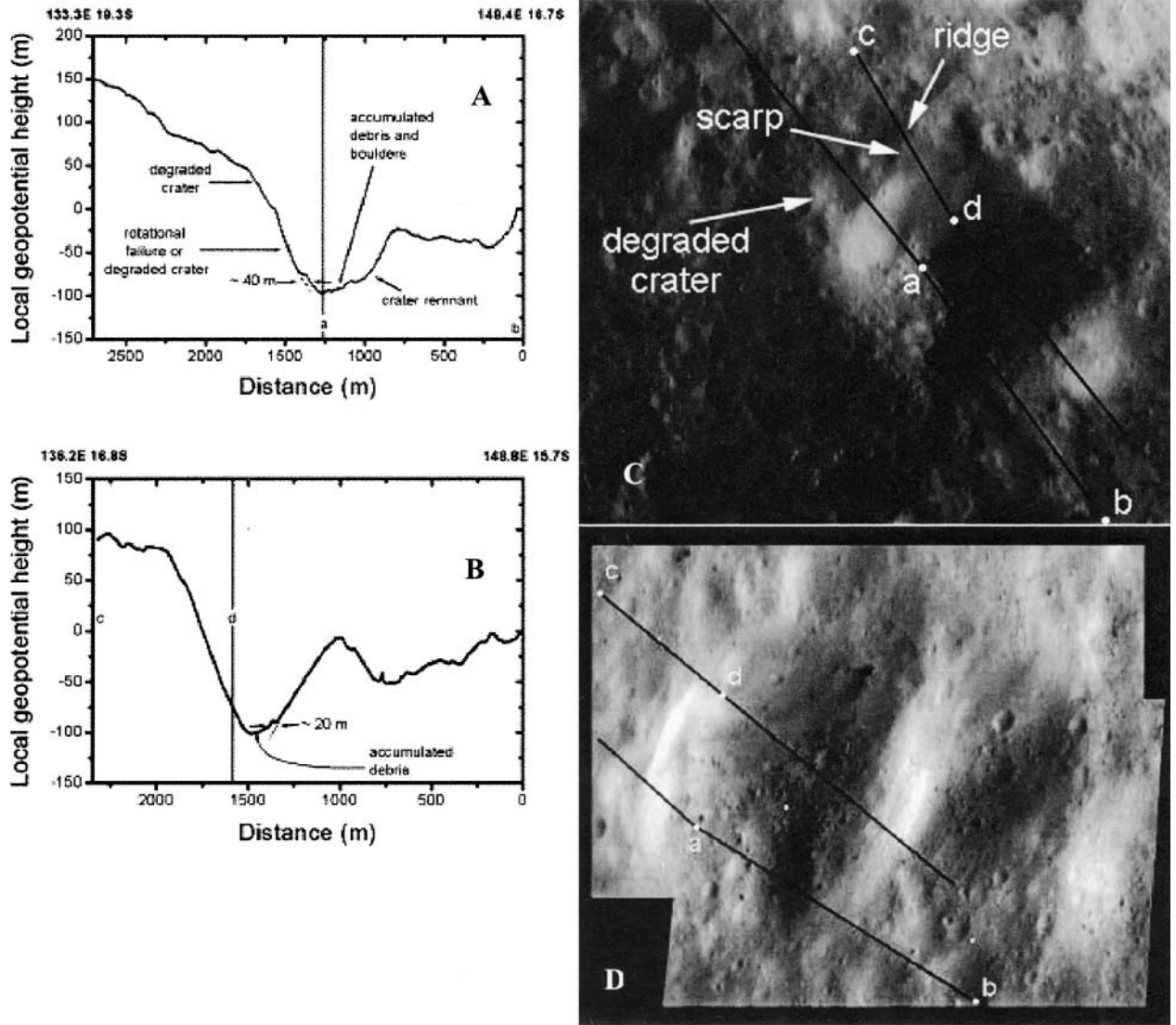
FIG. 10. A square crater southeast of Himeros. The NLR profiles (A) and (B) are in the format of Fig. 7. Points on the profiles are called out and marked on the images. The image (C) was taken at MET 132151598 on d117 from a range of 53 km. The mosaic (D) was compiled from images taken on d198 at METs 139151830 and 139152131 from a 35-km orbit.

cratering (Melosh 1989), where the collapsing rim material exploits the planes of weakness and creates walls that tend to parallel the joint trends. Alternatively, if impact-driven shocks are predominantly reflected by fracture planes, the impact-damaged zone may be confined and may produce a square crater with sides almost parallel to joint trends.

The NLR profiles in Figs. 10A and 10B provide further evidence for infilling of the crater. The "diameter" of the crater (rim to rim) is ∼870 m, but the depth inferred from Fig. 10A is about 83 m whereas that from Fig. 10B is much greater, about 137 m. As both tracks appear to be at comparable distances from the center of the crater, this difference suggests the presence of 54 m of infill. A possible rotational slump failure marked in Fig. 10A corresponds to the oval feature following the degraded crater in

Fig. 10C. The slide material to the lower left side of the crater has both blocky and relatively smooth areas as shown in Fig. 10D, suggesting that multiple episodes have occurred. Both NLR profiles display small features that may indicate the depth of individual deposits, the estimated thicknesses of which range from 20 to 40 m. The steepest slope in Figs. 10A and 10B equals 37°.

Figure 11 shows an NLR track from d143 over the rim and eastern wall of Psyche. Figure 11C, a mosaic from images taken on d063, shows Psyche in the western hemisphere of Eros and the location of the NLR track. As this track is relatively lengthy, it was reduced in four segments, a–j, j–k, k–m, and m–q. The geopotential height is plotted in Fig. 11A versus distance, determined independently from each segment and then concatenated. Point f marks approximately the subdued eastern rim
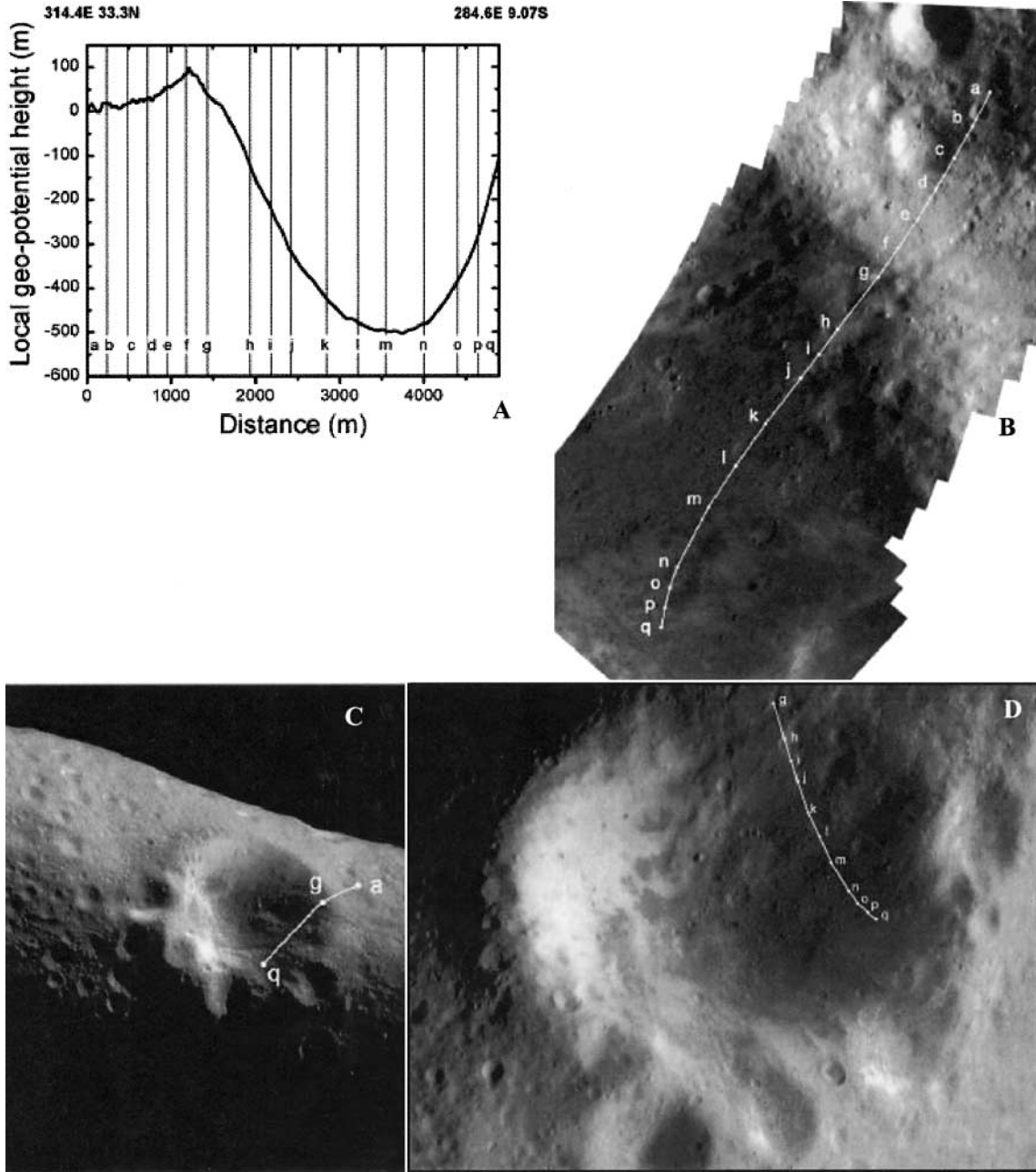
FIG. 11. Transect through crater Psyche. The NLR profile is plotted versus MET and versus distance in panel (A). Points are called out and are marked in images (B)–(D).

of Psyche. The NLR track does not descend to the floor of Psyche and therefore does not measure its full depth. A regional system of east–west trending grooves can be seen in Fig. 11C, going over the east rim of the crater and continuing across the crater, as can also be seen in Fig. 11B, which is a mosaic from the boresighted images obtained on d143 from 50-km orbit. Figure 11B shows that these grooves contain aligned chains of craters or pits. Also, these grooves are seen to branch, an observation which can be interpreted as reflecting the presence of intersecting systems of faults or fractures.

In Fig. 11B, the NLR track passes through a relatively fresh crater between a and b. Then it crosses a series of small grooves between b and d and at g which are almost orthogonal to the track in the image; these small grooves intersect the east–west trending grooves at a large angle. The east–west trending grooves also intersect the track around c, g, and j. From j to m in Fig. 11, the slope along the profile is shallower in a region where an increased number of large boulders is found. The profile between k and l passes through a small infilled crater similar to many others in this region of accumulated debris. After n the NLR profile
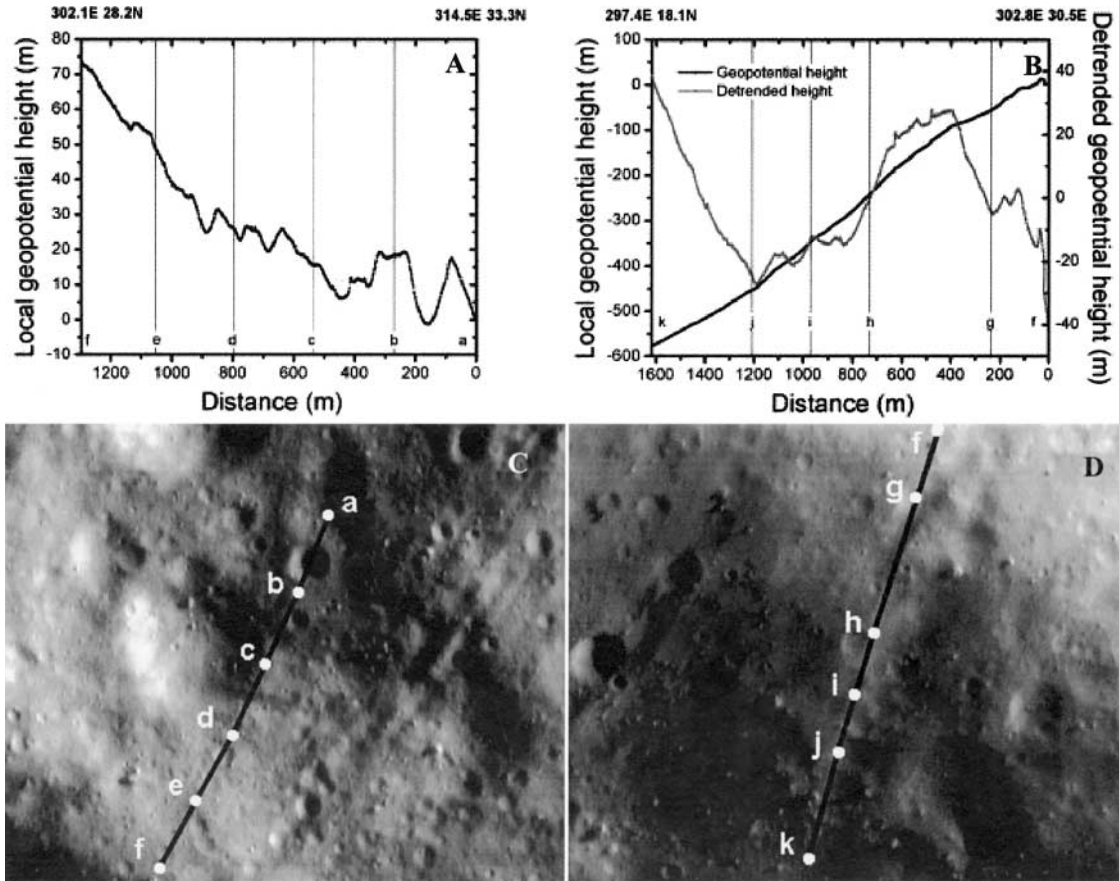
FIG. 12. Enlargements of Psyche transect in Fig. 11.

enters a third debris unit, in which the slopes along the profile are steeper and fewer boulders are found.

Figure 12 shows expanded views of this NLR track. The same points a–k are marked in Figs. 11 and 12. The near-rim region of Psyche is highly complex, and the boresighted images are indispensable to interpretation of the topographic profiles. The fresh crater transected between a and b (Fig. 12A) has a rim-to-rim diameter of 156 m and a depth-to-diameter ratio of 0.12. A series of shallower depressions is transected between b and d in Fig. 12A, but these are identified as grooves whose depth-to-width ratios range from 0.04 to 0.07. In addition to these grooves, a 10-m scarp is visible on the b side of the groove between b and c. A second crater is transected after d, but its depth-to-diameter ratio is less than the previous example at 0.10.

Point g in Fig. 12 is at the intersection of two groove systems. It is centered within one member of the orthogonal groove system also transected in b–d, but it is on the wall of the larger system of east–west trending grooves, accounting for the slope change after g in Fig. 12B (see the "detrended height" curve, which is geopotential height with a linear trend subtracted to bring out small features). The east–west trending groove which bifurcates as it enters Psyche has a depth of ∼20 m at g and a similar depth in its other branch at point j.

Structural features. Figures 13–16 present four examples of structural features on Eros, all of which are much larger than the small scarps and grooves discussed thus far. Figure 13 is an NLR track across the large system of ridges that define a "spiral" pattern southwest of Psyche, as shown in Fig. 13C (Veverka *et al.* 2000). These ridges are locally straight, like stripes on a barber pole, and follow approximate geodesics in the surface of Eros. The NLR profile in Fig. 13A was taken on d188, and the boresighted MSI image (cropped) is shown in Fig. 13B. The mosaic Fig. 13C was taken on d076. The NLR profile reveals that this feature consists of parallel cliffs separated by ∼600 m, with each cliff rising up to 130 m. The cliffs are sloped at up to 27° along the track, but the track is oblique to the cliff face. These data are suggestive of extensional tectonics.

Figure 14 shows another structural feature located at 116°E, 49°S southeast of Himeros. This observation was obtained on d154 from 47-km range, and the boresighted image was taken at MET 135340340. The image shows an elongated, curved trough that is part of a branching groove. The extension of this groove toward the lower left of the image cuts across the NLR profile between b and c, as evidenced by a subtle, linear brightness variation. The branching part of the groove system lies to the north and west of the NLR track, heading toward Himeros. The average slope from b to c is 6°, as shown by the geopotential
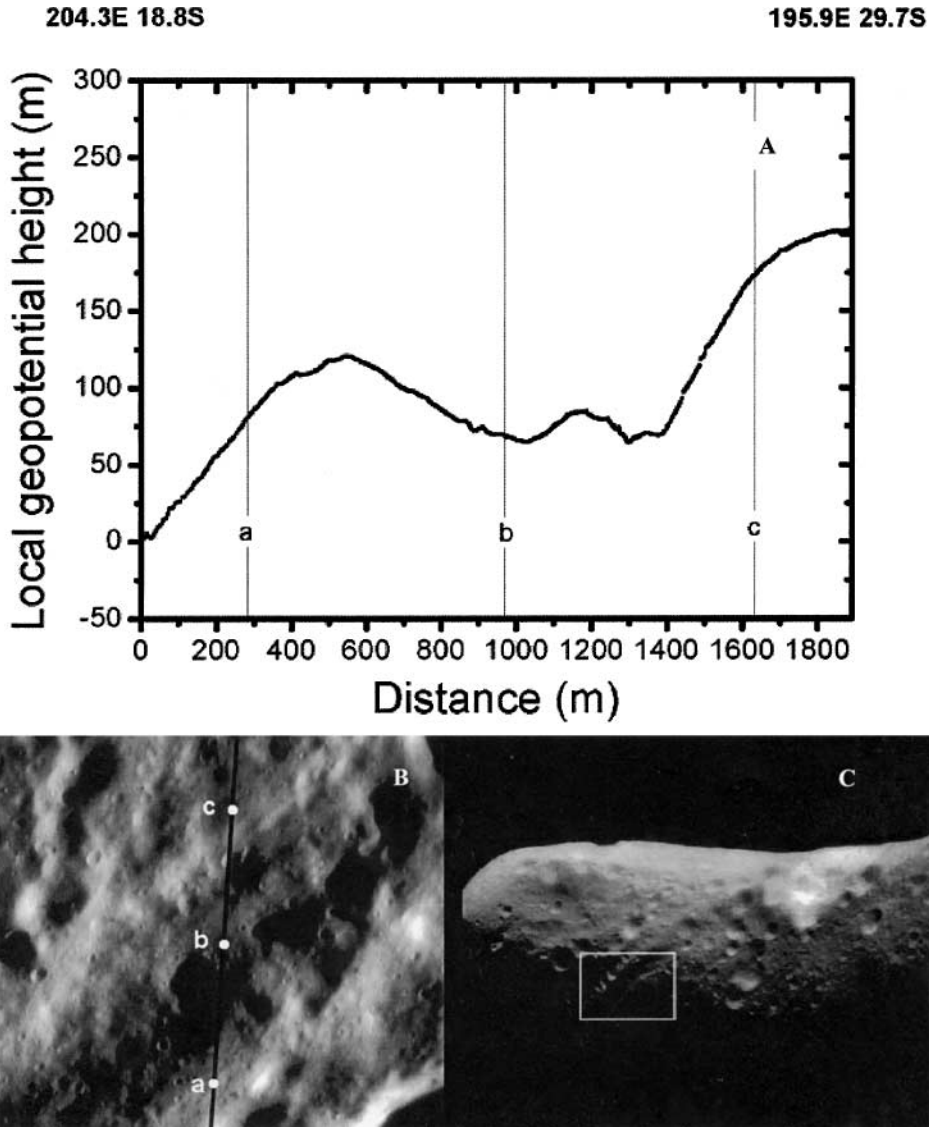
FIG. 13. The "spiral" feature southwest of Psyche. Panel (A) shows an NLR profile in the same format as in Fig. 7. Points are called out and marked in the boresighted image of panel (B), which was taken at MET 138258277 from a range of 47.5 km. The mosaic (C) was taken on d076 from MET 128615086 to 128615566. The NLR pass was obtained roughly within the boxed area.

height curve in Fig. 14A. A linear trend is removed to obtain the detrended geopotential height in Fig. 14A, from which the peak-to-trough topographic contrast is 24 m. The topographic profile suggests that the extension of the branching groove system away from Himeros is a ridge and groove system that can barely be discerned in the image.

Figure 15 shows a prominent ridge, on the opposite side of Himeros, that is one segment of a ridge system extending in total over 15 km on the surface of Eros (the Rahe Dorsum; Veverka *et al*. 2000). In the d091 mosaic of Fig. 15B, Himeros is to the lower right and is partly shadowed. The NLR profile in Fig. 15 was obtained on d116. The ridge morphology in the vicinity of the NLR track in Fig. 15, which was 13°E, 49°N, has been interpreted as consistent with compressional deformation (Veverka

et al. 2000). The NLR profile from a to f is also consistent with compression and further suggests a succession of fault blocks, e.g., one at or just before b and the next at c. The topographic contrast is 45 m from the peak to the bottom of the trough between points b and c.

Figure 16 shows structural features associated with the extension of this same prominent ridge system into Himeros. The region sampled in Fig. 15 can be seen at the upper left of the image in Fig. 16C; the large crater at the limb is the same crater that lies adjacent to the NLR track in Fig. 15C. The prominent ridge of Fig. 15 can be followed in Fig. 16C from this crater (called out in the image) into Himeros in the lower right, where two separate NLR tracks, labeled a′–f′ and a–j, are shown. The ridge becomes subtle before entering Himeros, where it becomes a system of
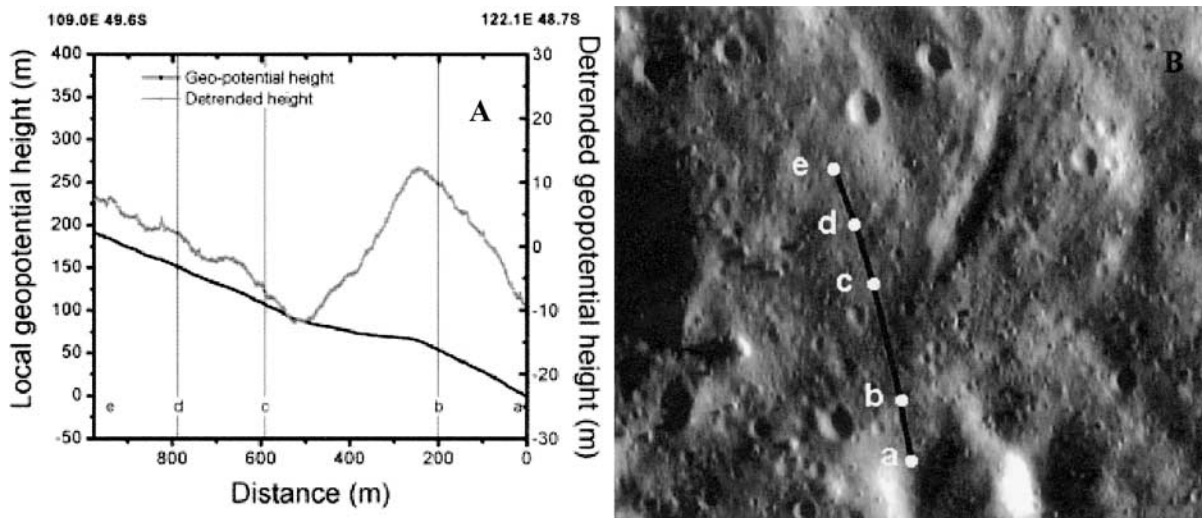
FIG. 14. Branching groove southeast of Himeros. The format is as in Fig. 7, except that the detrended geopotential height is plotted (right axis) in panel (A). The boresighted image in panel (B) was taken at MET 135340340 on d154 from 47-km range.
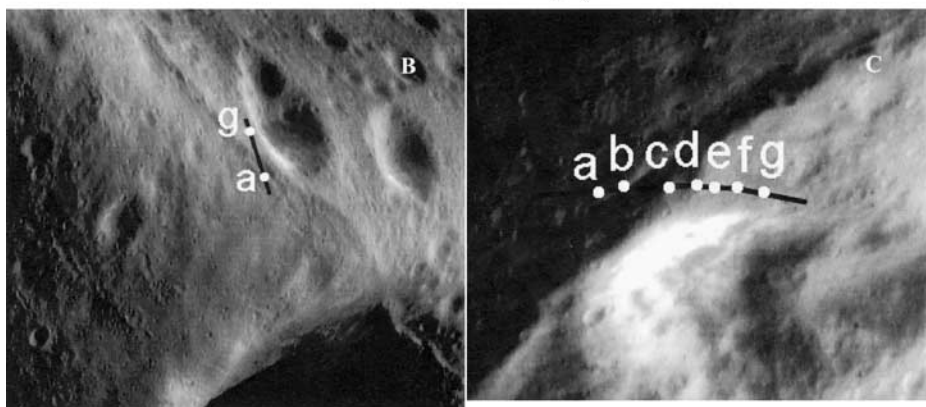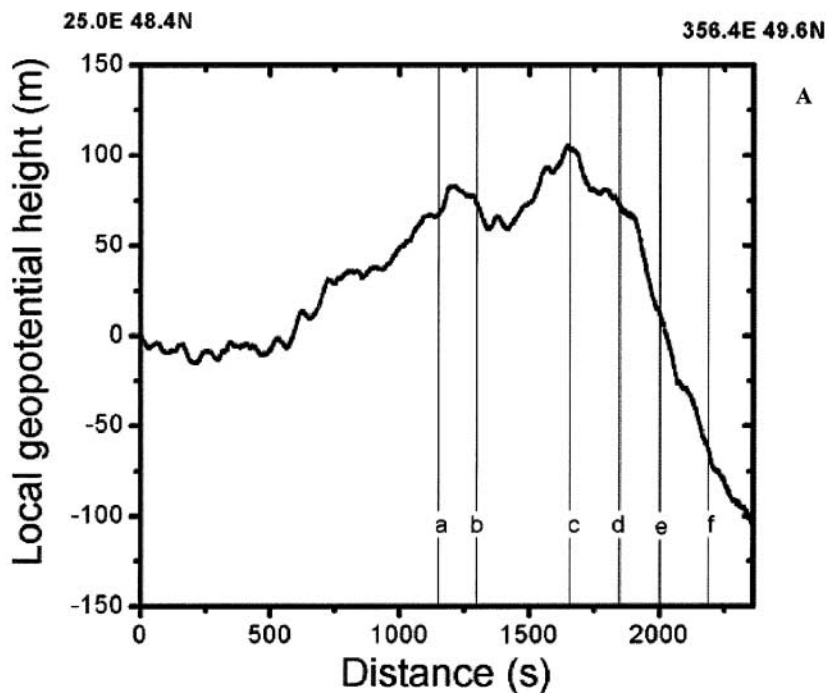

FIG. 15. Prominent ridge at northern latitudes near Himeros. The format is as in Fig. 7. The mosaic in (B) was obtained from 200-km orbit on d091. The boresighted image (cropped) in panel (C) was taken at MET 132051295 on d116 from a range of 91 km.
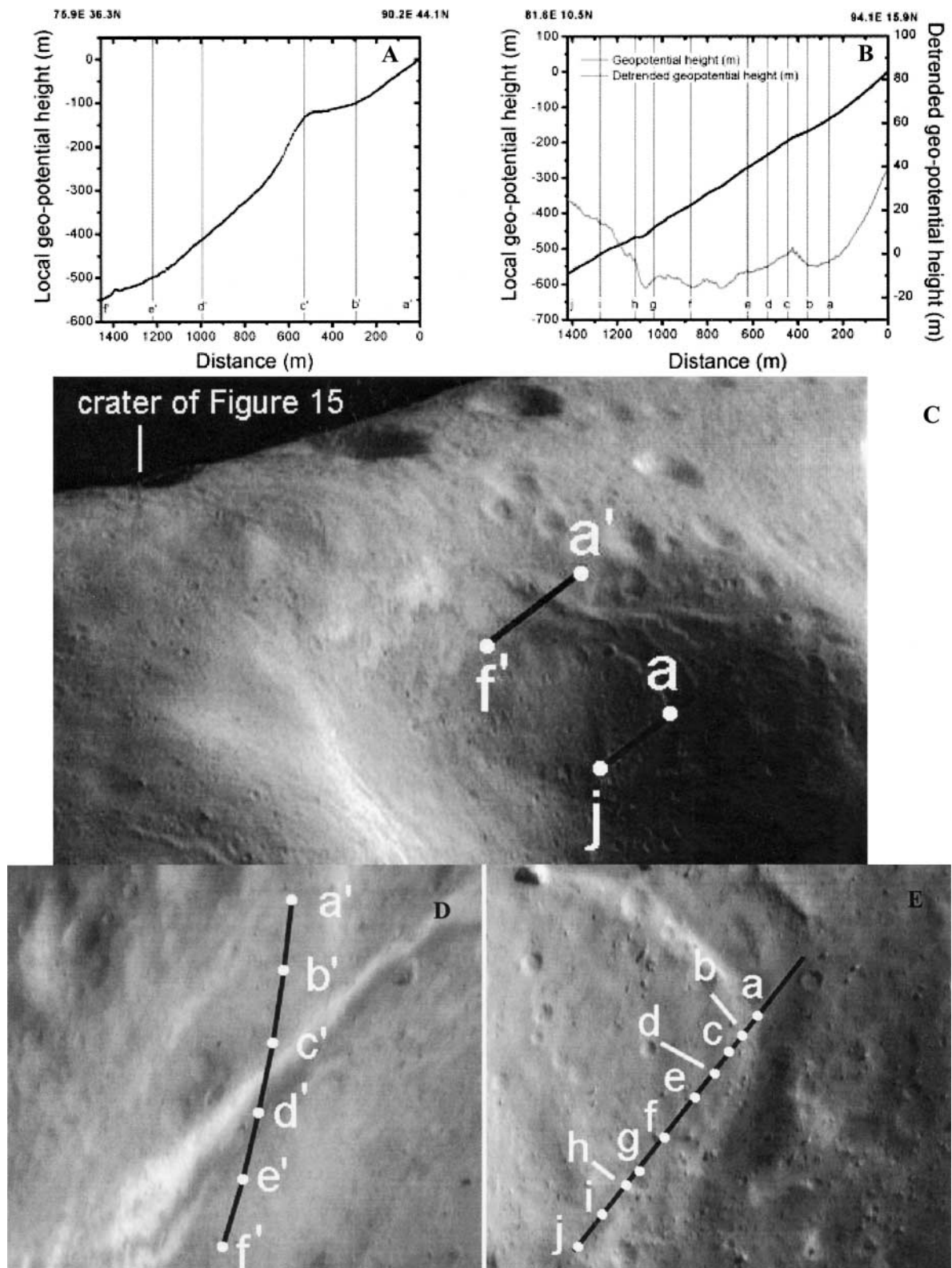
69

FIG. 16. Structural features in Himeros. The format is as in Fig. 7. The image in panel (C) was taken on d099 at MET 130615115 from 205-km range. In panel (D), the boresighted image (cropped) was taken at MET 135398509 on d154 from a range of 45.7 km, corresponding to the profile in panel (A). In panel (E), the boresighted image (cropped) was taken at MET 134012242 on d138 from a range of 45.7 km, corresponding to the profile (B).

branching ridges and troughs with flat floors. The NLR track a′–f′ in Fig. 16A was obtained on d154. The topographic profile (Fig. 16A) reveals the feature in Fig. 16D to be a spectacular cliff with an elevation change of >110 m. The slope of the cliff face, which appears bright in Fig. 16D because of the illumination and viewing conditions, has a slope of 46° measured along the track, which would exceed the likely angle of repose and imply that this feature is made of consolidated material.

The second track in Fig. 16B was obtained on d138. This track is on the eastern wall of Himeros and has an average slope of 23° from a to j. A shallow crater is transected in segment g–h, and another is transected in segment e–f. From the detrended geopotential height curve, the crater in g–h is 9-m deep and 106 m in diameter (depth/diameter ~ 0.09), while the e–f crater is 8-m deep and ~ 93 m in diameter (depth/diameter ~ 0.09), so both craters provide evidence for regolith infill. Nearly all the craters in Fig. 16E appear unusually shallow, suggesting that filling of craters has occurred throughout the region. A curving trough is seen in Fig. 16E that is part of the Rahe Dorsum system discussed above. The NLR track covers one wall of this trough, and a scarp is found close to c. Despite the spectacular appearance of this trough in images, it is surprisingly shallow, with only 10-m topography. This shallowness may also reflect presence of regolith infill. Consistent with this suggestion is that the slope in the apparently flat-bottomed trough is nearly equal to the average slope over the entire track.

Surface roughness. While it is already evident that Eros has an extremely irregular shape with a generally rough surface, it is desirable to quantify and to characterize this roughness, so that different regions on Eros can be compared and so that Eros can be compared with other bodies. The calculation of fractal surface statistics is a powerful tool for such characterization, as many planetary surfaces exhibit self-affine structure on scales of interest (Turcotte 1997, Shepard and Campbell 1998, Neumann and Forsyth 1995, Aharonson *et al.* 2000). In the following, individual NLR profiles are reduced to determine the standard deviation (square root of Allan variance) of height differences versus baseline L. The standard deviation is given by $\sigma = \langle [h(x) - h(x + L)]^2 \rangle^{0.5}$, where $h(x)$ is the geopotential height of a given sample in a track, with a linear trend removed, versus distance x. Here distance is defined as above, measured along the line that best fits the track. In a self-affine structure the standard deviation of height differences, measured for all pairs of samples in a track separated by a baseline L, obeys

$$\sigma = \sigma_0 (L/L_0)^H, \qquad (4)$$

where L_0 is always 1 m. The quantity H is called the Hurst exponent and is related to fractal dimension δ by the relation $\delta = 2 - H$. The quantity σ_0 is the normalizing constant.

Figure 17 presents this fractal statistic for six specific tracks, all of which have been discussed above. Figure 17A shows this fractal statistic for three segments of the Psyche crater transect shown in Fig. 11: the near rim and rim ranging from points

TABLE III
Fractal Statistics of Surface Roughness

Description	Hurst exponent H	σ_0 (m)	Reference
Himeros (Fig.16)	0.81	0.18	This study
Twist (Fig.13)	0.89	0.30	This study
Groove (Fig.14)	0.82	0.14	This study
Psyche rim (a–j; Fig.11)	0.91	0.35	This study
Psyche debris (j–n; Fig.11)	0.87	0.22	This study
Psyche wall (n–q; Fig.11)	0.87	0.23	This study
Black rock a′a flow	0.55	0.46	Shepard and Campbell (1998)
Mars Pathfinder terrain	~ 0.5	NA	Shepard and Campbell (1998)
Undisturbed lunar regolith	0.5–0.7	0.02–0.07	Helfenstein and Shepard (1999)

a to j, the blocky region between j and n, and the smoother crater wall between n and q. Figure 17B compares this statistic for the Himeros track in Figs. 16B and 16E, for the cliffs of the "spiral" region of Fig. 13; and for the branching groove of Fig. 14. Table III shows the fractal roughness statistics σ_0 and H for each of the six tracks analyzed.

It is noteworthy in Fig. 17 that approximately self-affine behavior is found over more than two decades of baseline length. The limit at the small scales is set by the footprint size and/or spacing, and it is limited at the large scales by the track lengths and/or large structural features. Hence, the true range of self-affine structure cannot be determined from these data; self-affinity may persist to much smaller scales. It is also noteworthy that the Hurst exponents are nearly the same for all six tracks, ranging from a minimum of 0.81 to a maximum of 0.91. This suggests that similar physical processes determine the surface morphology over all regions studied. The fractal statistics quantify how the twist region, with its huge cliffs, is rougher than subdued topography of the branching groove and Himeros: The roughness differences are expressed mainly as differences in the normalizing constant. Deviations from self-affine behavior in Fig. 17B at large baselines (>200 m) may reflect the influences of the structural features (ridges and grooves) targeted in these tracks.

Similar results are obtained from the Psyche tracks shown in Fig. 17A. The near-rim and rim track a–j is rougher than the other two tracks, debris (j–n) and wall (n–q), which were also noted to be smoother in the images. For all three profiles in Psyche and the twist profile in Fig. 17B, the roughness statistics are almost the same at small scales; the standard deviations of heights in all four tracks fall within a factor of 2 of one another at baselines below 100 m. This significant result is interpreted as reflecting the ubiquitous presence of cratering and regolith processes on Eros. The Himeros and groove tracks in Fig. 17B are smoother, with σ_0 reduced by less than a factor of 3 from the twist. The Himeros track was noted in images to exhibit infilling of craters.
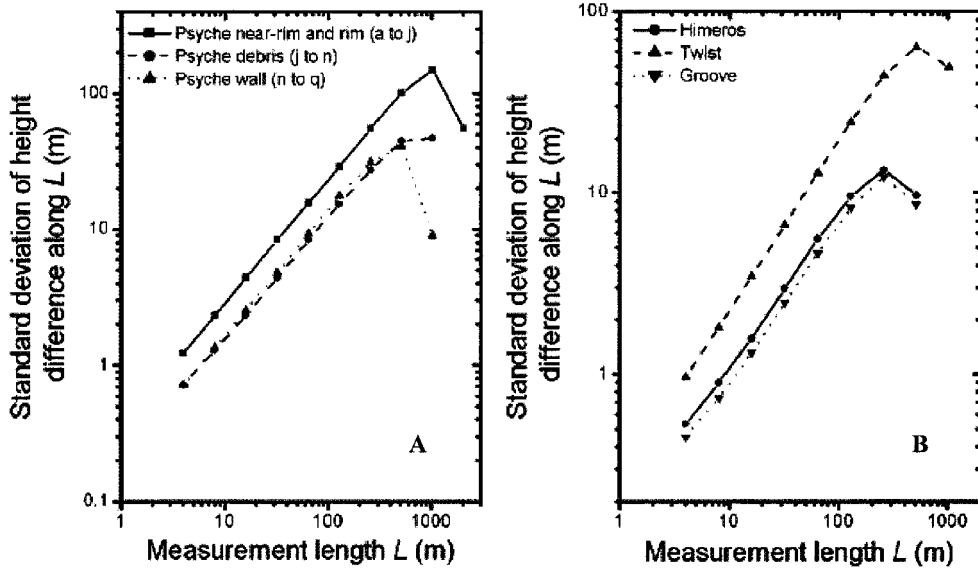
FIG. 17. Fractal statistics of six NLR profiles. The track labeled "twist" is the one in Fig. 13. The Hurst exponents and the normalizing constants from these profiles are listed in Table III.

Table III also compares the fractal statistics found for Eros with those reported for a terrestrial a'a lava flow, Mars Pathfinder terrain, and undisturbed lunar regolith (Shepard and Campbell 1998, Helfenstein and Shepard 1999). The a'a lava data over centimeter to meter scales and the lunar regolith data at submillimeter to centimeter scales have been converted to SI units as used in this study for ease of comparison. All of the six Eros tracks discussed above have a significantly larger Hurst exponent than those for the a'a lava, Mars terrain, and undisturbed lunar regolith, meaning that the roughness increases much faster with baseline distance on Eros than on the planet-sized bodies. A direct comparison of σ_0 in Table III is misleading because the self-affine regime on Eros is at larger scales than in the other cases. More meaningful is a comparison of the fractual slope σ/L, which scales as L^{H-1}. The fractal slope of Eros at 10-m scales is in the range of fractal slopes for lunar regolith at millimeter scales, and both of these are less than the value reported for the a'a lava on 10-cm scales. Because H at Eros is close to unity, the fractal slope scarcely decreases at larger scales. The surface of Eros is extremely rough.

7. CONCLUSIONS

This paper has reported initial results on small-scale topography of 433 Eros, using boresighted images to aid in the interpretation of altimetric profiles. The observations presented here comprise $\ll 1\%$ of the NLR data, and they do not represent a complete or an unbiased survey. They do illustrate the diversity of topographic features and are representative of the entire data set in terms of ranging precision and fractions of missing and noise returns.

The availability of simultaneous, boresighted images from NEAR MSI enables interpretations of individual NLR profiles prior to construction of high-resolution topographic grids. By restricting the analyses to short profiles of $\sim$2000-s duration, the relative topography of surface features can be studied to within the $\sim$1-m ranging precision despite the presence of larger absolute positioning errors, which are nearly constant over the course of a short profile and which therefore do not affect relative topography. The altimetric data provide valuable insights into the nature of surface features.

The results of this paper provide additional support to the conclusion of Yeomans *et al.* (2000), Veverka *et al.* (2000), and Zuber *et al.* (2000) that Eros is a consolidated body. There are extreme slopes on Eros, well above expected angles of repose, and a competent substrate must be present to support these slopes. There are structurally controlled craters and numerous tectonic features which also imply the presence of a competent substrate. At the same time, Eros has an unconsolidated surface layer that is subject to downslope motion. The depth of this layer is inferred in specific cases as typically a few tens of meters. These results have an interesting implication for the nature of cratering on Eros. In particular, craters on Eros larger than $\sim$100-m diameter would not be gravity controlled but would be formed in a fracture-controlled (Nolan *et al.* 1996) or strength-controlled regime. In support of this suggestion, it is noted that *if* Psyche formed in a gravity-controlled regime, *it alone* would provide a regolith cover of $\sim$40-m global average depth, which would presumably be unconsolidated and able to slide (since *any* crater ejecta falling back to the surface would impact at speeds below the escape velocity of 3–17 m/s). The relatively shallow depths of unconsolidated material as inferred here would be difficult

to understand if the larger craters on Eros formed in a gravity-controlled regime.

The surface of Eros has also been found to have a self-affine structure over scales from a few meters to hundreds of meters. The surface of Eros is very rough, especially at large scales, and the roughness as inferred from fractal statistics of NLR profiles correlates with the visual appearance of the surface. The fractal dimension of the surface is similar for diverse regions on Eros, suggestive of similar processes shaping the surface on observed scales in these regions.

APPENDIX

The plate model for the shape of Eros uses a triangular tessellation of the surface. It consists of a list of vertices, which are points on the surface of the asteroid, and associated data structures which define how these vertices are linked to form triangles approximating the surface. Each of these triangles is called a "plate." The plate model is constrained such that the areas of the individual plates do not differ from one another by more than about a factor of 2. In addition to the list of vertices, the plate model contains a list of plates with the identities of the vertices that form each plate. Also included in the plate model is a list of the nearest neighbors for each plate and a list of the latitude–longitude coordinates for the centroid of each plate.

The plate model vertices are written as

$$\mathbf{v}_m, \quad m = 1, \ldots, M,$$

where each vertex $\mathbf{v}_m$ is a Cartesian vector in asteroid body-fixed coordinates and is numbered by the index m for the total of M vertices. The NLR190 model has 3863 vertices. The plate centroids are defined by

$$\mathbf{R}_i = (\mathbf{v}_i + \mathbf{v}_j + \mathbf{v}_k)/3, \quad n = 1, \ldots, N_p,$$

where the plates are numbered by the index n for the total of N_p plates, and where vertices i, j, k form plate n. The NLR190 model has 7722 plates. Each plate is oriented such that its outward normal vector is

$$\mathbf{N}_n = (\mathbf{v}_j - \mathbf{v}_i) \times (\mathbf{v}_k - \mathbf{v}_i).$$

Here $\mathbf{N}_n$ is not a unit vector but is a surface element with dimensions of area and with magnitude equal to twice the area of the plate. The volume of the plate model, which approximates the volume of the asteroid, is then

$$V = \sum_n (\mathbf{N}_n \cdot \mathbf{R}_n)/6,$$

where the summation is over all plates. If the density of the asteroid is uniform, as is true to an excellent approximation of Eros (Yeomans *et al*. 2000, Zuber *et al*. 2000), then the center of mass coordinates are given by the vector

$$\mathbf{X}_{CM} = \frac{1}{4V} \sum_n \mathbf{N}_n (\mathbf{R}_n \cdot \mathbf{R}_n),$$

where again the summation is over all plates. If the density ρ is uniform, then the gravitational potential is

$$U(\dot{\mathbf{x}}) = \frac{G\rho}{4} \sum_n \frac{(\mathbf{x} - \mathbf{R}_n) \cdot \mathbf{N}_n}{|\mathbf{x} - \mathbf{R}_n|},$$

which is added to the centrifugal potential $-\Omega^2(x^2 + y^2)/2$ to obtain the geopotential. Here the volume integral in (2) is transformed to a surface integral and approximated as a summation over plates. The notation is the same as in (2). Also, the body axes are defined such that the rotation axis is $\mathbf{z}$. Eros is in principal axis rotation, within the limit of detectability (Yeomans *et al*. 2000). The formula applies inside or outside the volume, and the surface can be convex or concave. If $\mathbf{x} = \mathbf{R}_n$ omit that term from the sum.

REFERENCES

Aharonson, O., M. T. Zuber, and D. H. Rothman 2000. Statistics of Mars' topography from MOLA: Slopes, correlations and physical models, *J. Geophys. Res.* **106**, 23723.

Asphaug, E., J. M. Moore, D. Morrison, W. Benz, M. C. Nolan, and R. Sullivan 1996. Mechanical and geological effects of impact cratering on Ida. *Icarus* **120**, 158–184.

Bell, J. F., D. Davis, W. Hartmann, and M. Gaffey 1989. Asteroids: The big picture. In *Asteroids II* (R. Binzel, T. Gehrels, and M. Matthews, Eds.), pp. 921–945. Univ. of Arizona Press, Tucson.

Cheng, A. F., A. Santo, K. Heeres, J. Landshof, R. Farquhar, R. Gold, and S. Lee 1997. Near-Earth Asteroid Rendezvous: Mission overview. *J. Geophys. Res* **102**, 23695–23708.

Cheng, A. F., T. Cole, M. Zuber, D. Smith, Y. Guo, and F. Davidson 2000. Inflight calibration of the Near Earth Asteroid Rendezvous laser rangefinder. *Icarus* **148**, 572–586.

Cole, T. D., M. Boies, A. El-Dinary, A. F. Cheng, M. Zuber, and D. E. Smith 1997. The Near Earth Asteroid Rendezvous laser altimeter. *Space Sci. Rev.* **82**, 217–253.

Davis, D. R., E. Ryan, and P. Farinella 1994. Results from current scaling algorithms. *Planet. Space Sci.* **42**, 599–610.

Harris, A. W. 1998. A thermal model for near-Earth asteroids. *Icarus* **131**, 291–301.

Helfenstein, P., and M. Shepard 1999. Submillimeter-scale topography of the lunar regolith. *Icarus* **141**, 107–131.

Melosh, H. J. 1989. *Impact Cratering: A Geologic Process*. Oxford Univ Press, London.

Melosh, H., and E. Ryan 1997. Asteroids: Shattered but not dispersed. *Icarus* **129**, 562–564.

Murchie, S., and 17 coauthors 1999. Inflight calibration of the NEAR multi sectral images. *Icarus* **140**, 66–91.

Neumann, G. A., and D. W. Forsyth 1995. High resolution statistical estimation of seafloor fabric: The morphology of an evolving spreading center. *Mar. Geophys. Res.* **17**, 221–250.

Neumann, G. A., D. D. Rowlands, F. G. Lemoine, D. E. Smith, and M. T. Zuber 2000. Crossover analysis of MOLA altimetric data. *J. Geophys. Res.* **106**, 23753.

Nolan, M. C., E. Asphaug, H. Melosh, and R. Greenberg 1996. Impact craters on asteroids: Does gravity or strength control their size? *Icarus* **124**, 359–371.

Ostro, S., and 19 colleagues 1999. Radar and optical observations of Asteroid 1998 KY26. *Science* **285**, 557–559.

Ostro, S., R. S. Hudson, M. Nolan, J.-L. Margot, D. Scheeres, D. Campbell, C. Magri, J. Giorgini, and D. Yeomans 2000. Radar observations of Asteroid 216 Kleopatra. *Science* **288**, 836–839.

Quaide, W. L., and V. R. Oberbeck 1968. Thickness determinations of the lunar surface layer from lunar impact craters. *J. Geophys. Res.* **73**, 5247–5270.

Scheeres, D. 1995. Analysis of orbital motion around 433 Eros. *J. Astronaut. Sci.* **43**, 427–452.

Shepard, M., and B. Campbell 1998. Shadows on a planetary surface and implications for photometric roughness. *Icarus* **134**, 279–291.

Shoemaker, E. M. 1963. Impact mechanics at Meteor Crater, Arizona. In *The Moon, Meteorites and Comets* (B. M. Middlehurst and G. P. Kuiper, Eds.). Univ. of Chicago Press, Chicago and London, 301–336.

Smith, D. E., M. T. Zuber, G. A. Neumann, and F. G. Lemoine 1997. Topography of the Moon from the Clementine LIDAR. *J. Geophys. Res.* **102**, 1591–1611.

Smith, D. E., M. T. Zuber, S. C. Solomon, R. J. Phillips, J. W. Head, J. B. Garvin, W. B. Banerdt, H. V. Frey, D. O. Muhleman, G. H. Pettengill, G. A. Neumann, F. G. Lemoine, J. B. Abshire, O. Aharonson, C. D. Brown, S. A. Hauck, A. B. Ivanov, P. J. McGovern, H. J. Zwally, and T. C. Duxbury 1999. The global topography of Mars and implications for surface evolution. *Science* **284**, 1495–1503.

Smith, D. E., M. T. Zuber, H. V. Frey, J. B. Garvin, J. W. Head, D. O. Muhleman, G. H. Pettengill, R. J. Phillips, S. C. Solomon, H. J. Zwally, W. B. Banerdt, T. C. Duxbufy, M. P. Golombek, F. G. Lemoine, G. A. Neumann, D. D. Rowlands, O. Aharonson, P. G. Ford, A. B. Ivanov, P. J. McGovern, J. B. Abshire, R. S. Afzal, and X. Sun 2000. Mars Orbiter Laser Altimeter (MOLA): Experiment summary after the first year of global mapping of Mars. *J. Geophys. Res.* **106**, 23689.

Thomas, P., J. Veverka, D. Simonelli, P. Helfenstein, B. Carcich, M. Belton, M. Davies, and C. Chapman 1994. The shape of Gaspra. *Icarus* **107**, 23–36.

Thomas, P., M. Belton, B. Carcich, C. Chapman, M. Davies, R. Sullivan, and J. Veverka 1996. The shape of Ida. *Icarus* **120**, 20–32.

Turcotte, D. L. 1997. *Fractals and Chaos in Geology and Geophysics.* Cambridge Univ. Press, Cambridge.

Veverka J., and 16 colleagues 1997a. NEAR's flyby of 253 Mathilde: Images of a C Asteroid. *Science* **278**, 2109–2114.

Veverka, J., and 12 colleagues 1997b. An overview of the NEAR multispectral imager-near-infrared spectrometer investigation. *J. Geophys. Res.* **102**, 23709–23727.

Veverka, J., and 25 colleagues 1999. Imaging of Asteroid 433 Eros during NEAR's flyby reconnaissance. *Science* **285**, 562–564.

Veverka, J., and 32 colleagues 2000. NEAR at Eros: Imaging and spectral results. *Science* **289**, 2088–2097.

Yeomans, D., and 12 colleagues 1997. Estimating the mass of Asteroid 253 Mathilde from tracking data during the NEAR flyby. *Science* **278**, 2106–2109.

Yeomans, D., and 15 colleagues 2000. Radio science results during the NEAR Shoemaker spacecraft rendezvous with Eros. *Science* **289**, 2085–2088.

Zuber, M. T., D. E. Smith, F. G. Lemoine, and G. A. Neumann 1994. The shape and internal structure of the Moon from the Clementine mission. *Science* **266**, 1839–1843.

Zuber, M. T., D. E. Smith, A. F. Cheng, and T. Cole 1997. The Near laser ranging investigation. *J. Geophys. Res.* **102**, 23761–23773.

Zuber, M., and 11 colleagues 2000. The shape of Eros from the NEAR-Shoemaker laser rangefinder. *Science* **289**, 2097–2101.